Case Studies in Thermal Engineering 47 (2023) 103058

Contents lists available at ScienceDirect

Case Studies in Thermal Engineering

journal homepage: www.elsevier.com/locate/csite

Case study of autocatalysis reactions on tetra hybrid binary nanofluid flow via Riga wedge: Biofuel thermal application

Tanveer Sajid [a], Abdullatif A. Gari [b], Wasim Jamshed [a,*], Mohamed R. Eid [c,d], Nazrul Islam [b], Kashif Irshad [e], Gilder Cieza Altamirano [f], Sayed M. El Din [g]

[a] Department of Mathematics, Capital University of Science and Technology (CUST), Islamabad, 44000, Pakistan
[b] Department of Mechanical Engineering, King Abdulaziz University, Jeddah, 21589, Saudi Arabia
[c] Department of Mathematics, Faculty of Science, New Valley University, Al-Kharga, Al-Wadi Al-Gadid, 72511, Egypt
[d] Department of Mathematics, Faculty of Science, Northern Border University, Arar, 1321, Saudi Arabia
[e] Interdisciplinary Research Centre for Renewable Energy and Power System (IRC-REPS), Research Institute, King Fahd University of Petroleum and Minerals (KFUPM), Dhahran, 31261, Saudi Arabia
[f] Universidad Nacional Autónoma de Chota, Cajamarca, Perú Fizmako Research Group, Bogotá, Colombia
[g] Center of Research, Faculty of Engineering, Future University in Egypt, New Cairo, 11835, Egypt

ARTICLE INFO

Handling Editor: Huihe Qiu

Keywords:
Wedge-shape geometry
Cross nanofluid
Inclined magnetic field
Heat transport
Chemical process via *Autocatalysis*

ABSTRACT

Ethanol and biodiesel, which both belong to the first generation of biofuel technology, are the two most popular forms of biofuels now in use. In order to create next-generation biofuels using waste, cellulosic biomass, and algae-based resources, the Bioenergy Technologies Office (BETO) is working with business. The present article is designed to study the effect of tetra hybrid nanoparticles with the utilization of the novel Hamilton and Crosser model and catalytic reaction on binary fluid with the consideration of ethanol biofuel as a base fluid. Ethanol comprising tetra hybrid nanoparticles and heterogeneous catalytic reaction amplifies thermal conductivity and significantly increases brake thermal efficiency and reduces brake-specific fuel consumption in diesel engines. Therefore, the aim of this article is a theoretical checkup that is related to heat and mass transport of biofuel flow considering binary fluid accompanied with autocatalysis reaction and novel tetra hybrid nanoparticles on biofluid flow subjected to a Riga wedge. Transportation of heat via nonuniform heat source/sink, thermal radiation, and thermal conductivity are in our consideration. The mathematics of the assumed problem generates the system of non-linear partial differential equations from basic equations of momentum, energy, and mass. The usage of non-dimensional variables gave a system of non-linear ODEs with boundary conditions which are further dealt with in the Lobatto111A scheme. The results are obtained for stretching/shrinking wedge with several parameters. From obtained results, it is observed that the velocity field diminishes owing to magnification in Weissenberg number and Casson fluid parameter. The temperature field diminishes by amplifying heat generation, thermal radiation, and variable thermal conductivity parameter. Concentration distribution escalates by rising homogeneous reaction parameters.

* Corresponding author.
E-mail address: wasiktk@hotmail.com (W. Jamshed).

https://doi.org/10.1016/j.csite.2023.103058
Received 27 March 2023; Received in revised form 6 May 2023; Accepted 10 May 2023
Available online 11 May 2023

1. Introduction

The current world is facing the massive challenge that ordinary fluids have low thermal conductivity, due to this fact researchers kept their attention to this problem. To address this issue nanofluid healed this gap by transport of heat. Nanofluid is the suspension of nano-sized particles 100 nm in size. Currently, many experimental studies are established on this heat transference of nanofluids, and existing studies witnessed that nanofluids brought massive improvement in thermo physical traits, like viscosity density and thermal conductivity. Solid particles have been employed in the field of industrial process and engineering, for instance, titanium oxide, silver, alumina, copper, gold, silica, etc. These fluids have a high capacity for heat transference and are widely utilized in practical problems, for example, peristaltic pumps for diabetic treatment, cancer therapy, temperature reduction, electronic cooling, solar collectors, etc. Choi [1] used the notion of nanofluids through the combination of base liquid with solid nanoparticles. Lee et al. [2] did the experimental analysis and showed that nanoparticle suspension promotes the heat transport properties of water. After this analysis, Buongiorno [3] predicted the thermal conductivity mechanism of nanomaterials with the assumption of thermophoretic diffusion along Brownian movement. Reddy et al. [4] published their examination with double diffusion combined effects, mixed convection, and MHD flow of nanofluids caused by disturbing an infinite plate. Khan and Pop [5] chose the same path to expose a numerical study of the laminar flow of nanofluids generated through a flat plate which was cable of being stretched along the effects of Brownian motion and thermophoresis. Influence of magnetic field on Al_2O_3–water nanofluid is predicted by Sheikholeslami et al. [6]. Mutuku-Njane and Makinde [7] did find the Newtonian heating effect with a nanofluid permeable stretching sheet. Mabood et al. [8] explored the impact of viscous dissipation on magnetized nanofluids and achieved a numerical solution to the proposed model. Computation of considered multiple solutions found by Khan and Hafeez [9] with slip condition and nanofluid flow with the transport of heat. Khan et al. [10] achieved a numerical solution of fluid accompanied by copper nanoparticles. Ma et al. [11] did numerical findings that convective heat transport in nanofluids through a channel is the most effective transportation. Hamid et al. [12] utilized a mathematical model of Williamson liquid with the geometry of a vertical surface and they made computations about numerical solutions. Mahanthesh [13] investigated the impact of quadrative radiative heat flux and nanoparticles on fluid with the utilization of a modified Buongiorno nanofluid model. Khan et al. [14] looked at the effect that organisms but also nonlinear dependent radiative heat phenomena might have on Burgers nanoliquid. The influence of cubic autocatalysis chemical reaction on Oldroyd-B fluid accompanied by variation in thermal conduction phenomenon was scrutinized by Irfan et al. [15].

There seems to be a great deal of investigation further into the manufacture of contemporary nanofluids; these kinds of fluids are thought to those as ternary nanofluids (THNFs). THNFs have enhanced heat transfer characteristics as a consequence of the associations of several constituents, which has a cumulative effect on the system as a whole. Researchers all over the world investigated ternary hybrid nanofluid due to its better heat transfer rate in comparison to ordinary hybrid nanofluid. Adun et al. [16] investigated various aspects of ternary hybrid nanofluid and their effect on fluid. Sneha et al. [17] conducted an in-depth examination of the influence that ternary nanocomposites have now upon radiative couple stress liquid traveling through a permeable material. Goud et al. [18] investigated variable thermal conductivity impact on THNFs moving inside the dovetail fin. Nasir et al. [19] investigated THNF impact on magnetized couple stress liquid. Cao et al. [20] scrutinize mixed convective THNFs embedded with radiate heat flux and surface slip phenomena. The effect of stagnation points on magnetized ternary hybrid nanofluid past a cylinder having a convectively heated surface embedded with a heat source as well as the suction effect was investigated in detail by Mahmood et al. [21]. Researchers led by Krishna and colleagues [22] looked at how ternary polymeric nanoparticles affected biomagnetic liquid so that it flowed around the wedge and achieved the solution of the proposed model with the utilization of MANFIS method. Sajid et al. [23] scrutinized the impact of ternary hybrid nanoparticles accompanied by binary chemical reaction and activation energy on nanofluid past a wedge. The effect of tetra hybrid nanoparticles on Cross fluid flow through stenosis arteries with the inclusion of effects like non-uniform heat source-sink and thermal radiation were investigated in detail by Sajid et al. [24]. The influence of Cattaneo- Christov heat flux and nonlinear type of heat source/sink on tetra hybrid Reiner-Philippoff fluid moving subjected to a stretchable sheet were investigated deeply by Sajid et al. [25]. Guan et al. [26] observed that the insertion of nanoparticles in the base fluid amplifies the thermal conductivity of the fluid and heat transfer amplifies more in the case of hybrid nanofluid in contrast to simple nanofluid. Wang et al. [27] scrutinized the effect of an electrical field on nanoliquid and found that an exchanging electrical current practical in a microchannel can enhance the heat transference by up to about 20% compared with DC electrical current. The impact of thermo magnetic convection and thermophoresis effect on Fe_3O_4-water based nanofluid with the utilization of a modified Buongiorno model was investigated in detail by Wang and Yuan [28]. Wang et al. [29] presented a literature review on how the heat transference rate of nanofluid amplifies as it is exposed to electric and magnetic fields.

An electromagnetic sheet known as a “Riga plate” is where electrodes are alternately built. Electromagnetic hydrodynamic behavior in the fluid flow is produced by this configuration. Managing the intensity of the electric and magnetic fields stabilizes the fluid’s velocity. The notion of developing a wall-parallel Lorentz force was first proposed by Latvia [30]. A set of aligned spanwise alternating electrodes and permanent magnets made up the electromagnetic actuators that Gailitis and Lielausis utilized to regulate the flow of fluids in their device design. Researchers across the world investigated the Riga effect on fluid flow subjected to various geometries like plates, and wedges. Abdal et al. [31] investigated hybrid nano-liquid accompanied by activation energy phenomenon on tangent hyperbolic nanoliquid. Yahya et al. [32] numerically achieved the solution of tangent hyperbolic liquid across a Riga wedge. The dual solutions of Ag–MgO/water hybridity nanoliquid flowing across an expanding/constricting Riga wedge and stagnating region are expressed by Basha et al. [33]. Habib et al. [34] inspected the Riga effect on Prandtl nanofluid moving subjected to a wedge and solved the modeled problem numerically with the exploitation of the well-established Keller box method. The effect of fuzzy nanoparticles on the flow of a second-rate hybrid nanoliquid towards a Riga wedge is shown by Imran et al. [35]. A micropolar nanoliquid flow across an expanding wedge in the presence of an applied magnetic field was studied by El-dawy et al. [36].

For more than many decades, interest has been found in fluid flow subjected to wedge by several authors and it helps in growing mass transport under the influence of activation energy through the wedge. Such flows do challenge our engineering abilities and keep themselves as the most appropriate demanding faculties because they have applications, like, spinning of filaments, crude oil extraction, storage of nuclear waste, geothermal systems, insulation phenomenon in thermal science, heat exchangers design, etc. For the elaboration of the Prandtl boundary layer theory, Falkner [37] did an investigation with 2-D laminar flow passing through Falkner's wedge. They proposed equations for the investigation of fluid flow. Thereafter, with this exciting invention of stretching/shrinking wedge many scholars did work on different physical effects; see Refs. [38–42]. Moreover, magnetized fluid flow with heat transport considering wedge having pores in it is discussed by Xu and Chen [43]. Condensing of pores medium with a constant wedge is utilized by Sayyed et al. [44] and he saw the impact of the slip velocity condition in the presence of a magnet regime. Investigation about the dual solution and heat transferring/generation over the geometry of stretching/shrinking wedge is made by Awaludin et al. [45]. Viscous dissipation and Lorentz force effect on nanofluid passing through wedge along with the phenomenon of heat transport is revealed by Ibrahim and Tulu [46].

Term catalysis is the substance that initiates a chemical reaction to happen differently. The presence of catalysis makes a faster chemical reaction as compared to the usual reaction. Mass transport via chemical processes has now been used in biological structures. A chemical reaction is classified into two types: homogeneous and heterogeneous reactions. A reaction that occurs in a single phase is homogeneous and occurs in two or more phases called a heterogeneous chemical reaction. Both reactions are not gradually or collectively deprived of catalyst. These chemical processes have the competency to react faster with catalysts. Few studies on these chemical processes related to diffusion, and fog materialization were examined via Merkin [47]; Xu et al. [48]; Hayat et al. [49]. The chemical specie mechanism with second-grade fluid was explored by Imtiaz et al. [50] and the chemical reactive process with ferromagnetic reactive was done by Waqas [51] and who depicted those homogeneous/heterogeneous parameters fall off the concentration of micropolar fluid.

Using various conversion methods, biorefinery is a sustainable method for turning biomass feedstock into biofuels and other bioproducts. A large part of the renewable energy sources that go into creating a carbon-neutral energy system is biofuel. By maximizing the carbon cycle on our planet, biofuels contribute to a reduction in the carbon footprint of the transit and other the manufacturing sector. Each gallon of biofuel that is used in place of a gallon of fossil fuel reduces greenhouse gas emissions. By accelerating the earlier start of burning and reducing igniting delay in biodiesel, nanomaterials reduce the pressure in the cylinder at full capacity and the rate at which heat is released. It is noted that the addition of different types of nanoparticles in the base fuel. The use of NPs significantly increases brake thermal efficiency and reduces brake-specific fuel consumption in diesel engines and this phenomenon is much better in the case of the agglomerative type of tetra hybrid nanoparticles in contrast to ternary ad hybrid nanoparticles. In the past, when catalysts were used to make biodiesel, they made waste products like soap, glycerol, and a lot of water that couldn't be used. Catalysts seem to be effective in resolving nearly all such problems. The latest technological advances make use of innovative, heterogeneous catalysts derived from biomass and waste materials. Many studies have demonstrated how heterogeneous catalysts obtained from biomass may be used to generate significant, purified ethanol in an even more environmentally friendly way [52–56].

As was already said, biodiesel is often made by *trans*-esterifying oils from animals, plants, or oleaginous pathogens, along with alcohol like ethanol [57]. But this method has a few major problems, the most important of which are saponification, the loss of catalysis, and a slow rate of reaction [58]. Hence, experts think that nanotechnology can indeed be efficiently employed to tackle these issues. In recent years, nanoscience has risen to prominence as a game-changing technology with far-reaching implications [59]. Nanomaterials, which have many interesting and innovative features, are always the foundation of the nanotechnology field. It has been stated that the surface area of nanoparticles, including metallic nanoparticles, can be several hundred times higher than that of macroscopic-scale substances with a comparable weight. In addition to a massive rise in surface area, researchers discovered several other improved attributes while examining nanostructures [60–62]. Current improvements in nanotechnology and certain significant research indicate that the prospective catalyst effectiveness of nanomaterials makes them one of the most attractive catalysts for biofuel generation, notably in biodiesel production. To this day, numerous nano-based common or synthesized as well as characterized heterogeneous catalysts possessing tremendous catalytic attributes like high activity, chemical stability, high porosity, a substantial surface area, etc. have been synthesized and are employed in the biodiesel manufacturing process [63]. According to the hypothesis put forth by Kumar et al. in their study [64], a conventional heterogeneous catalyst would typically be composed of a relatively small number of nanoparticles that are already scattered over a high porosity substance that has a surface area ranging approximately from 250 m^2/g. Nanocatalysts deployed mostly in the manufacture of biodiesel include metal oxides such as CaO, MgO, Fe_3O_4, Cu/Al/-TiO_2/SiO_2/Al_2O_3, and SnO_2 [65,66].

1.1. Process of making biofuel (waste food stock)

Effective biodiesel can make use of a broad range of organic waste, opening up exciting new avenues for production strategies and biofuel applications. Organic waste encompasses materials from the following sectors: agriculture, woods, cellulosic trash, wildlife, creatures, paper and plastic, sewage, and hazardous effluent. Raw material made from bits of organic business trash is common and cheap in urban areas. Conversely, agricultural crop debris and much other vegetal garbage are more suitable for agricultural biofuel production. This waste material is transported into a processing unit for making biofuel.

1.2. Biofuel production unit

1.2.1. Milling

After every grain husk has been dried and processed into a "meal" in some kind of dry mill, the "meal" gets slurred, adding water, to

produce a "mash." The starch in the mash is broken down into sugar either by adding enzymes or by fermentation. After being processed, the mash gets chilled before being delivered to the fermentation processes. When yeast is introduced, sucrose starts to ferment into alcohol.

1.2.2. Saccharification

Saccharification is indeed the name given to the process that involves grinding to convert starches into sucrose as well as dextrin (from the Greek, "to make into sugar"). The hydrolysis of cellulose in maize starches helps in the creation of fermentation of processed sugar but also unfermentable dextrin. This procedure leads to the production of brew, which seems to be a saccharine solution through which beer is produced.

1.2.3. Fermentation

During the fermentation procedure, yeast, which is a monoculture microbe, is introduced to a slurry. The decomposition of glucose by yeast is indeed an important step in the biological reaction known as fermentation. Glucose is the energy source for yeast. The end outcome is the production of ethanol.

1.2.4. Transportation

Ethanol produced is further stored in large iron drums and transported to biofuel pumping stations with the help of trucks and large containers.

1.2.5. Biofuel pump

In the end, biodiesel is delivered to biofuel pump filling stations.

1.3. Future of biofuel in Pakistan

The United Nations predicts Pakistan's population to be 198, 139, 348 as well as growing by 1.97% per year. Energy is used at the following rates: 45.7% for residential use; 7.5% for commercial usage; 28.1% for farm needs; 11.8% for lighting purposes; 5.6% for commodity supplies. Throughout Pakistan, agriculture is responsible for 21% of GDP across all important crops, secondary crops, poultry, aquaculture, and forests. The contributions of the primary, secondary, poultry, and wood industries towards GDP are 5.3%, 2.3%, 11.8%, and 0.4%, correspondingly. Pakistan's agricultural sector has been its main supplier industry. The lack of reliable power sources is a major barrier to economic development in Pakistan as well as other primary and secondary agricultural products including rice, wool, grain, but also sugarcane. The power crisis in Pakistan also hampers the growth of its economy.

1.3.1. Energy situation and effects responsible for the energy crisis in Pakistan

The Hydrocarbon Development Institute of Pakistan has indeed backed up important numbers for the energy sector (HDIP). In 2022, oil (30.8%), methane (49.5%), charcoal (87.4%), and liquefied petroleum gas (0.5%) accounted for 80.8% of the natural assets used, while energy obtained through water (10.5%), nuclear energy (1.9%), plus purchased energy (0.1%) comprised the other 12.5%. As much as 33–35% of Pakistan's GDP is lost due to the country's 6000 MW supply gap. Pakistan is home to about 55 million people, yet only around 35% of them have access to power. On average, power outages endure 6–12 h per day in urban areas, but 12–18 h per day in rural areas. Factors like electricity theft, shortage of gas, expensive oil as well as oil shortage, and lack of efficient policy regarding energy distribution are the main reasons for the energy crisis in Pakistan. Resources like oil, gas, and electricity are decreasing day by day due to much dependence on these sources.

1.3.2. Utilization of renewable sources in Pakistan

What we call "renewable power" comes through resources that naturally regenerate at a faster pace than when we use them. Examples of these kinds of renewable resources comprise sunshine, air, biomass, waste of plants and trees, etc. The world is teeming with alternatives for energy from natural ways (pollutant free). Pakistan is an agricultural country with an agricultural area of 22.68 (million hectares). The main crops are wheat, cornflower, sugar cane, etc. Pakistan ranked 9th in sugarcane production. There is great potential to produce biofuel from waste products in Pakistan. Ethanol production in Pakistan is not new. The fermentation process is used to produce ethanol from sugarcane. The current manufacturing capability of gasoline-quality ethanol within Pakistan is 270,000 tons annually, even though the country does have the possibility of making 400,000 tons annually.

1.3.3. How to meet this deficiency?

Six million plants would've been farmed on 5000 acres of ground, yielding 24 million kilos of seed per year as well 7.2 million gallons of biodiesel, under the program of Pakistan state oil (PSO). Arable land covers just 22.1% (or 22.1 million) of a country's 79.6% of the entire area of land; the remainder is made up of non-arable waste, heavily forested areas, including marshy lands. Farmers improve their economic status through the cultivation of oil-seed-bearing vegetation. Farmers have been urged to cultivate 57.5 million hectares of undeveloped land by farming crops from which oil is extracted as much as possible. Formerly unusable terrain owing to water scarcity or soil salinity could be cultivated to produce oil. Growing energy commodities would be good for farmers and the country's economy.

1.4. Purpose of the current study

1.4.1. Existing literature

A few years ago, several numerical/analytical studies have been demonstrated for inquiry related to boundary layer flow, analysis of heat transport, and reactive chemical flow with Cross fluid bearing nanoparticles accompanied with homogeneous/heterogeneous

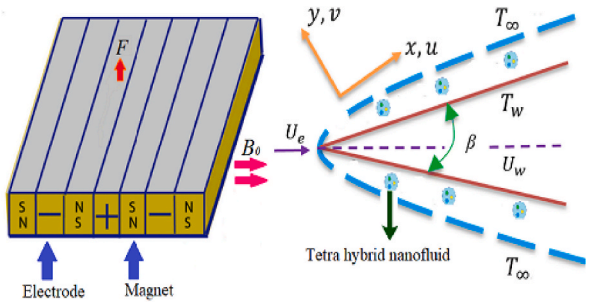

Fig. 1. Geometrical representation of flow model.

reaction effect. In almost all cases authors considered the fluid accompanied by homogeneous and heterogeneous reaction flow over different stretching surfaces like stretching disks, channels, vertical cones, and contracting/expanding cylinders and evaluated their solutions.

1.4.2. Research gap

In light of the above-mentioned literature and existing literature, no effort has been made to investigate the effect of homogeneous/heterogeneous reaction on any sort of non-Newtonian fluid moving subjected to expanding/contracting wedge. No effort has been made in the existing literature to develop a model accompanied by tetra nanoparticles. The theme of the current study is to discuss the solutions for Casson-Cross nanofluids flow subjected to Riga wedge under mass transport but also heat deliver phenomenon.

1.4.3. Motivation

The present is designed to investigate the effect of homogenous/heterogeneous chemical reactions on Casson-Cross nanofluid flow towards a porous wedge. Heat and mass transfer analysis is carried out with the inclusion of various effects like heat generation, homogeneous/heterogeneous (HO/HH) chemical reaction, and tetra hybrid Hamilton and Crosser nanofluid flow over a Riga wedge. The impact of tetra hybrid nanoparticles on ethanol base fluid has been investigated deeply in this article. Tetra hybrid nanoparticles' impact is studied on bioethanol considered a base fluid.

1.4.4. Novelty

The goal of this investigation is to examine how Casson-Cross nanofluid is affected by HO/HH reactions it flows through a porous wedge accompanied by thermal radiation, thermal conductivity, heat generation, and HO/HH reactions. The article is novel in its sense that the effect of homogeneous/heterogeneous in the case of any non-Newtonian fluid past a porous wedge accompanied with tetra hybrid nanoparticles has never been explored yet in the existing literature. Tetra nanoparticles like $Cu/Al/TiO_2/SiO_2/Al_2O_3$ amplify heat transfer rate and thermal conductivity and production of bioethanol up to 59.96%.

2. The geometry of the statement

Let us assume that there is a steady, 2-D, and incompressible flow of cross nanofluids flowing over a stretching/shrinking wedge under the influence of an inclined magnetic field as shown in Fig. 1. Ethanol is considered a base fluid and the addition of nanoparticles in sugar cane waste amplifies the fermentation process and more ethanol is generated. Energy transport has been hashed up with the existence of heat generation. Underneath the assumption of autocatalysis, an isobaric chemical mechanism is used to examine the phenomena of mass transport. Consider a thermostatic reaction with autocatalysis E as well as F, respectively.

$$E + 2F \rightarrow 3F, and\ rate = k_1 G_a G_b{}^2 \tag{1}$$

but also, the one-order adiabatic response upon that surface of catalysts is defined as

$$E \rightarrow F, and\ rate = k_s G_a \tag{2}$$

It's important to keep in mind that the impact here on the wedge's edge occurs even when $rate = k_s G_a G_b{}^2$ zero distance from the playing surface. G_a and G_b represent the concentrations for chemical species E and F, correspondingly; k_s and k_1 represent the rates of HO and HH reactions. Catalytic reactions elevate the fermentation process and saccharification process during which starches are transformed into sucrose. The physical model for nanofluid flow and coordinate axes are indicated in the geometry mentioned in Fig. 1. $x-$ axis has been in the same direction as the wedge sheet, and even the $y-$ axis is normal to the $x-$ axis. Fluid is subjected to an inclined magnetic field having its variable strength $B(x) = B_0 x^{m-1/2}$, where B_0 shows steady magnetic field strength. $U_w(x) = ax^m$ is the velocity distribution for (stretching/shrinking) wedge, and $a > 0$ constant of the stretching wedge but when $a < 0$ it tells the shrinking behavior of the wedge. Moreover, non-uniform velocity distribution $u_e = bx^m$ is the outermost edge velocity of the boundary layer with constant b, m is the viscosity symbol known as the parameter of Falkner–Skan and keeps its range in $m \in [0, 1]$ where $m = \beta/2 - \beta, \beta = \Omega/\pi$ represents the angle of the wedge. The temperature/concentration of nanoparticles with the surface of stretching/shrinking wedge are being assumed as T_w, C_w and T_∞, C_∞ are ambient (temperature/concentration) respectively.

Assumptions.

Table 1
Thermophysical properties.

Properties	Ethanol	SiO_2	TiO_2	Cu	Al_2O_3
ρ	789	3970	4250	8933	3970
C_p	2460	765	690	385	765
k	0.17	36	8.953	400	40

- Calculations (3) through (7) which are employed in modeling, were obtained from the principles of mass conservation and the second principle of motion by using Navier Stoke's calculation, the second principle of thermodynamics, and Fick's second principle.
- Incompressible laminar cross nanofluid is moving over an expanding/contracting wedge.
- Magnetized Riga wedge is considered in the present problem to study the effect of the magnetic field. The magnetic field affects fermentation as well as the quality of ethanol produced. The sensory profile showed more residual sugar, faster fermentation, and purification of ethanol.
- Novel Hamilton and Crosser tetra hybrid nanofluid is developed and considered in the present problem.
- Ethanol is considered as a base achieved after the fermentation of sugar cane and cornflower and the addition of nanoparticles in sugar cane or cornflower product accelerates the fermentation process and delivers more ethanol.

Now mathematics of this model takes place as bellow [27,32,43,47].

$$\frac{\partial u}{\partial x}+\frac{\partial v}{\partial y}=0, \tag{3}$$

$$u\frac{\partial u}{\partial x}+v\frac{\partial u}{\partial y}=u_e\frac{du_e}{dx}+\frac{\mu_{tethnf}}{\rho_{tethnf}}\left\{\left(1+\frac{1}{\beta}\right)\frac{\partial^2 u}{\partial y^2}+\frac{\partial}{\partial y}\left[\frac{\frac{\partial u}{\partial y}}{1+\left(\Gamma\frac{\partial u}{\partial y}\right)^n}\right]\right\}+\frac{j_0M_0\pi}{8}exp\left(\frac{\pi}{d}y\right)-\frac{\mu_{tethnf}}{\rho_{tethnf}}\left(\frac{u-u_e}{k^*}\right), \tag{4}$$

$$u\frac{\partial T}{\partial x}+v\frac{\partial T}{\partial y}=\frac{1}{\left(\rho C_p\right)_{tethnf}}\left[\frac{\partial}{\partial y}\left(k_{tethnf}(T)\right)\frac{\partial T}{\partial y}\right]+\frac{Q^*(T-T_\infty)}{\left(\rho C_p\right)_{tethnf}}-\frac{1}{\left(\rho c_p\right)_{tethnf}}\frac{\partial q_r}{\partial y}, \tag{5}$$

$$u\frac{\partial G_a}{\partial x}+v\frac{\partial G_a}{\partial y}=D_A\frac{\partial^2 G_a}{\partial y^2}-k_1G_aG_b{}^2, \tag{6}$$

$$u\frac{\partial G_b}{\partial x}+v\frac{\partial G_b}{\partial y}=D_B\frac{\partial^2 G_b}{\partial y^2}+k_1G_aG_b{}^2. \tag{7}$$

Physical BCs are linked with the system of PDEs

$$\left.\begin{aligned} u=u_w(x),v=v_w(x),T=T_w,D_A\frac{\partial G_a}{\partial y}=0,D_B\frac{\partial G_b}{\partial y}=-k_sG_b \text{ at } y=0\\ u\to U_\infty,G_a\to G_\infty,T\to T_\infty,G_b\to 0,\text{as } y\to\infty, \end{aligned}\right\} \tag{8}$$

Velocity component $=(u,v)$, density $=\rho$, kinematic viscosity $=\nu$, relaxation time $=\Gamma$, power law index $=n$, specific heat $=C_p$, mass flux time-dependent viscosity $=\nu_w(x)=\nu_0x^{-\left(1-\frac{m}{2}\right)}$ and heat releasing/absorbing parameter $=Q=Q_0\,x^{-(1-m)}$ and β_0 indicates volumetric thermal expansion, D_A and D_B are species diffusivity of chemical species G_a and G_b respectively.

TETHNF Hamilton and Crosser nanofluid model are bestowed by Refs. [17,18]:

$$\left.\begin{aligned} &\mu_{tethnf}=\frac{\mu_f}{(1-\varphi_1)^{2.5}(1-\varphi_2)^{2.5}(1-\varphi_3)^{2.5}(1-\varphi_4)^{2.5}},\\ &\rho_{tethnf}=\left[(1-\varphi_1)\left\{(1-\varphi_2)(1-\varphi_3)\left[(1-\varphi_4)\varphi_f+\rho_4\varphi_4\right]+\rho_3\varphi_3+\rho_2\varphi_2\right\}+\rho_1\varphi_1\right],\\ &\left(\rho C_p\right)_{tethnf}=(1-\varphi_1)\left\{(1-\varphi_2)(1-\varphi_3)\left[(1-\varphi_4)\left(\rho C_p\right)_f+\left(\rho C_p\right)_{s_4}\varphi_4\right]+\left(\rho C_p\right)_{s_3}\varphi_3+\left(\rho C_p\right)_{s_2}\varphi_2\right\}+\left(\rho C_p\right)_{s_1}\varphi_1,\\ &\frac{k_{tethnf}}{k_{thnf}}=\frac{k_4+2k_{thnf}+2\varphi_4\left(k_4-k_{thnf}\right)}{k_4+2k_{thnf}+\varphi_4\left(k_{thnf}-k_4\right)},\frac{k_{thnf}}{k_{hnf}}=\frac{k_3+2k_{hnf}+2\varphi_3\left(k_3-k_{hnf}\right)}{k_3+2k_{hnf}+\varphi_3\left(k_{hnf}-k_3\right)},\\ &\frac{k_{hnf}}{k_{nf}}=\frac{k_2+2k_{nf}+2\varphi_2\left(k_2-k_{nf}\right)}{k_2+2k_{nf}+\varphi_2\left(k_{nf}-k_2\right)},\frac{k_{nf}}{k_f}=\frac{k_1+2k_f+2\varphi_1\left(k_1-k_f\right)}{k_1+2k_f+\varphi_1\left(k_f-k_1\right)}. \end{aligned}\right\} \tag{5}$$

Thermophysical properties of ethanol, SiO_2 TiO_2, Cu, and Al_2O_3 type of nanoparticles on ethanol as delineated in Table 1.

Several factors have led to the widespread use of silicon dioxide coatings, including the fact that it makes nanoparticles more soluble without changing their chemical makeup. TiO_2 has a vast surface area, making it a potent oxidizing agent with significant

photocatalytic activity. It is a cheap material with a high dielectric constant and low manufacturing expenses. Due to its high ductility, adaptability, thermal and electrical conductance, and durability against corrosion, it is a significant manufacturing metal. It is a nutrient that must be included in our everyday diet. Aluminum oxides and metals like copper have higher thermal conductivities than the majority of other liquids or solids made of non-metallic components. The addition of nanoparticles like Alumina and Copper in a base fluid amplifies the heat transfer rate much better in contrast to any other nanoparticles. The reason behind choosing these four types of nanoparticles is SiO_2 possesses a porousness construction, and very great adsorbing properties, TiO_2 possesses a stronger catalytic activity and both alumina and copper are excellent thermal conductors.

3. Transformation

By introducing the following suitable transformations:

$$\eta = y\sqrt{\frac{U_\infty (m+1)}{2\nu_f}}x^{(m-1)/2}, (T_w - T_\infty)\theta(\eta) + T_\infty = T, G_a = G_\infty \varphi(\eta), G_b = G_\infty \vartheta(\eta), \tag{9}$$

Expressions regarding velocity u but also v are

$$u = U_\infty x^m \frac{df}{d\eta}, v = -\left\{\frac{(1+m)\nu_f U_\infty}{2}\right\}^{\frac{1}{2}} x^{\frac{m-1}{2}}\left[f(\eta) + \left(\frac{m-1}{m+1}\right)\eta\frac{df}{d\eta}\right] \tag{10}$$

The possibility of flow is checked by the continuity equation, so the above transformations are valid for flow. By using them we get:

$$\left\{\left(1+\frac{1}{\beta}\right)\left[1+We^n\left(\frac{d^2f}{d\eta^2}\right)^n\right]^2 + \left[1+(1-n)We^n\left(\frac{d^2f}{d\eta^2}\right)^n\right]\right\}\frac{d^3f}{d\eta^3} + \left[1+We^n\left(\frac{d^2f}{d\eta^2}\right)^n\right]^2\left\{A_1A_2\left(f\frac{d^2f}{d\eta^2}\right) + \frac{2m}{(m+1)}A_1A_2\left[1-\left(\frac{df}{d\eta}\right)^2\right] - \frac{2\lambda}{m+1}\left(\frac{df}{d\eta}-1\right)\right\} + A_1A_2M\, exp(-\alpha\eta) = 0, \tag{11}$$

$$\left\{\left[(1+\varepsilon\theta) + \frac{4}{3A_4}Rd\right]\frac{d^2\theta}{d\eta^2} + \varepsilon\left(\frac{d\theta}{d\eta}\right)^2\right\} + Pr\left[\frac{A_3}{A_4}f\frac{d\theta}{d\eta} + \frac{Q}{A_4}\theta\right] = 0, \tag{12}$$

$$\frac{d^2\varphi}{d\eta^2} + Sc\left(f\frac{d\varphi}{d\eta} + k_2\varphi\vartheta^2\right) = 0, \tag{13}$$

$$\frac{1}{\delta}\frac{d^2\vartheta}{d\eta^2} + Sc\left(f\frac{d\vartheta}{d\eta} + k_2\varphi\vartheta^2\right) = 0. \tag{14}$$

In most practical cases concentration of species D_A and D_B are equal so $\delta = 1$. Using the relation for simplification $\varphi + \vartheta = 1$, so above (13–14) took the form

$$\frac{d^2\varphi}{d\eta^2} + Scf\frac{d\varphi}{d\eta} - Sck_2\,\varphi(1-\varphi)^2 = 0. \tag{15}$$

The transformation made the conversion of BCs of PDEs into ODEs, so they are

$$\left.\begin{aligned} f(0) = f_w, \frac{df(0)}{d\eta} = \varepsilon, \theta(0) = 1, \frac{d\varphi}{d\eta}(0) = Ks\varphi(0) \\ \frac{df(0)}{d\eta} \to 1, \theta(\infty) \to 0, \varphi(\infty) \to 1, \end{aligned}\right\} \tag{16}$$

Here 'ε' responds by stretching the wedge for ($\varepsilon > 0$) and shrinking the wedge for ($\varepsilon < 0$). Involved parameters are magnetic parameter $M^2 = 2\left(\frac{\sigma {B_0}^2}{x^{m-1}\rho b(m+1)}\right)$, Weissenberg number (Local) is $We^2 = \left(\frac{1}{2\nu}\right)[x^{3(m-1)}\Gamma(m+1)b^3]$, suction injection parameter is $f_w = \sqrt{2\left(\frac{\sigma}{\rho b(m+1)}\right)}$, $Ks = \sqrt{2\left(\frac{\nu}{b(m+1)}\right)x^{1-m}}\left(\frac{k_s}{D_A}\right)$ is diffusion coefficient. Further, heat generation parameter $Q = \frac{Q_0}{b(m+1)\rho c_p}$, Schmidt number $Sc = \frac{\nu}{D_B}$ and $k_2 = \left(\frac{2k_1G_\infty}{x^{m-1}(m+1)}\right)$ is the strength coefficient of homogeneous reaction with the rate coefficient of homogeneous reaction k_1. To get the solution with the help of the similarity variable we make substitution $= \frac{1}{3}$, so the final form of the Weissenberg number is $We^2 = \left(\frac{2\Gamma b^3}{3\nu x^2}\right)$. The mathematical calculations for physical quantities are described bellow

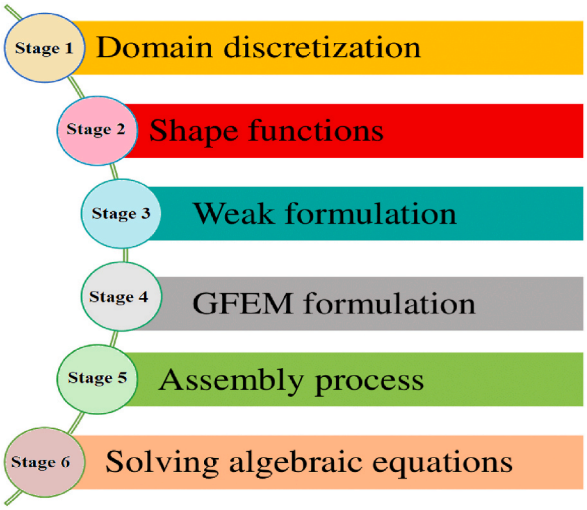

Fig. 2. Block diagram of GFEM scheme.

$$\left.\begin{aligned} C_{fx} = \left[\frac{\tau_w}{\rho U_w^{\,2}}\right], Nu_x = \left[\frac{xq_w}{k(T_w - T_\infty)}\right], \\ \tau_w = \mu_{tethnf}\left(\frac{\partial u}{\partial y}\left\{\frac{1}{1+\left(\Gamma\frac{\partial u}{\partial y}\right)^n}\right\} + \left(1+\frac{1}{\beta}\right)\frac{\partial u}{\partial y}\right), q_w = -k_{tethnf}\frac{\partial T}{\partial y}, \\ (Re_x)^{0.5}C_{fx} = \frac{1}{A_1}\left[\frac{(m+1)}{2}\right]\left(\left(1+\frac{1}{\beta}\right) + \left[\frac{1}{\left[1+\left(We\frac{d^2f(0)}{d\eta^2}\right)^n\right]}\right]\right)\frac{d^2f(0)}{d\eta^2}, \\ (Re_x)^{-0.5}Nu_x = -A_4\left[\frac{(m+1)}{2}\right]\left(\frac{d}{d\eta}(\theta(0))\right) \end{aligned}\right\} \quad (17)$$

where $Re = \frac{bx^{m+1}}{\upsilon}$, C_{fx}, Nu_x are Reynolds's number, skin friction and Nusselt number, respectively. Friction drag sometimes referred to as skin friction drag, is resistance felt by an item traveling across a fluid as it meets its surface. It grows with the square of the velocity and is exactly proportional to the area of the surface in contact with the fluid. The skin friction coefficient is linked with viscosity. It is observed that a positive variation in viscosity provides resistance to the flow and amplifies the skin friction coefficient. The skin friction coefficient is an important factor in fluid flow which decides how viscous the fluid is. Nusselt number is an important number in terms of determining the mode of heat transfer having important utilization in engineering applications. Nusselt number is the ratio of convective heat transfer to conductive heat transfer having important utilization in fluid flow. Higher values of the Nusselt number indicate that heat is transferred by convection instead of conduction. A positive variation in the Nusselt number amplifies the heat transfer rate. Insertion of nanoparticles in base fluid amplifies the Nusselt number phenomenon.

Proper attribution of the non-dimensional heat delivery rate lies with

Table 2
Exploration of rapidity and temperature in 300 un-mesh elements.

elements	$f'\left(\frac{\xi_{max}}{2}\right)$	$\theta\left(\frac{\xi_{max}}{2}\right)$
30	0.5962593	0.04215237
60	0.5963623	0.03912048
90	0.5967222	0.03551609
120	0.5969452	0.03268413
150	0.5226428	0.03229249
180	0.5225721	0.03197420
210	0.5223205	0.03154432
240	0.5125420	0.03126482
270	0.5101463	0.03056188
300	0.5072574	0.03026085

Table 3
Comparison analysis with existing literature.

m	Ref. [32]	Ref. [34]	Ref. [35]	Present
0	0.46960	0.4696	0.469601	0.46965
0.1	0.65497	0.6550	0.587036	0.58711
0.2	0.80212	0.8021	0.774754	0.77469
0.3	0.92765	0.9277	0.92768	0.92761
1	1.23258	1.2326	1.232587	1.23250

$$Nu_x Re_x^{-1/2} = -A_4(1+Rd)\theta' \tag{18}$$

whereas A_1, A_2, A_3, A_4 are given by

$$\left.\begin{aligned}
&A_1 = (1-\varphi_1)^{-2.5}(1-\varphi_2)^{-2.5}(1-\varphi_3)^{-2.5}(1-\varphi_4)^{-2.5},\\
&A_2 = (1-\varphi_1)\left\{(1-\varphi_2)(1-\varphi_3)\left[(1-\varphi_4)+\varphi_4\frac{\rho_4}{\varphi_f}\right]+\varphi_3\frac{\rho_3}{\varphi_f}+\varphi_2\frac{\rho_2}{\varphi_f}\right\}+\varphi_1\frac{\rho_1}{\varphi_f},\\
&A_3 = (1-\varphi_1)\left\{(1-\varphi_2)(1-\varphi_3)\left\{(1-\varphi_4)+\frac{(\rho C_p)_{s_4}}{(\rho C_p)_f}\varphi_4\right\}+\frac{(\rho C_p)_{s_3}}{(\rho C_p)_f}\varphi_3+\frac{(\rho C_p)_{s_2}}{(\rho C_p)_f}\varphi_2\right\}+\\
&\frac{(\rho C_p)_{s_1}}{(\rho C_p)_f}\varphi_1,\\
&A_4 = \frac{k_{tethnf}}{k_f}
\end{aligned}\right\} \tag{19}$$

4. Numerical solution

The boundary conditions associated with the current structure are theoretically recreated through the implementation of a finite element algorithm. The finite element method (FEM) is a technique that has demonstrated that it is very helpful when it comes to the process of resolving a wide range of complex issues. The method is being applied to the study of many issues about CFD dynamics. The notion that the required domain should be broken up into components is the core concept that underpins the finite element method (FEM). The FEM is indeed the topic of discussion throughout this study. Fig. 2 includes a discussion of the workflow for FEM technique. The following is a list of the advantages that this strategy offers. It is used in a variety of CFD problems nowadays.

Step 1: The very first stage involves the construction of remnants and indeed the formation of the weak form first from the dominant form.
Step 2: Throughout the second stage of the procedure, the outline parameters were occupied linearly, and now a weak form is generated by employing the Galerkin FE technique (GFEM).
Step 3: The third phase includes the building of a global stiffness matrix and indeed the construction of stiffness components via employing a particular assembly procedure.
Step 4: Throughout the fourth phase, an algebraic network is built employing the Picard linearization technique.
Step 5: Utilizing the preceding faltering circumstances, mathematical computations are imagined employing $10^{(-5)}$, which is (computationally broadmindedness): $\left|\frac{\eta_{i+1}-\eta_i}{\eta^i}\right| < 10^{-5}$..
Step 6: Somewhere in the sixth phase, the overall results of computation were presented using graphs as well as tables.
Step 7: However, at point VII, the native COSMOL Multiphysics® program is put to just use. Use FEM to solve the problem that has been studied.
Step 8: The method of resolving equations begins with the resolving of a system of equations, which is related to a stage 300 items model that carries out just the equation-handling procedure (Table 2).

5. Validity

The validation of obtained results and proposed numerical scheme are scrutinized by taking a comparison with existing literature [32,34,35] in the case of skin friction coefficient by taking $We = 0$, $n = 1$, $\beta \to \infty$ by changing wedge parameter m in Table 3. After doing an in-depth review of the relevant current literature, it has become abundantly evident that the suggested numerical approach, in addition to the findings that were produced, is both extremely advantageous and reliable.

6. Entropy generation

The mathematical form of entropy is swayed by

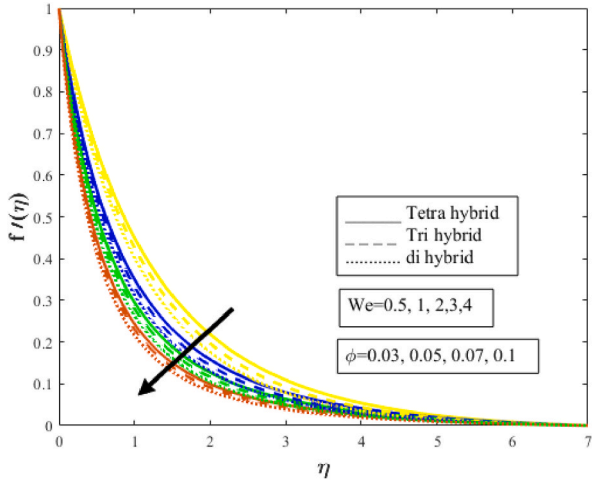

Fig. 3(a). Velocity profile $f'(\eta)$ decreases by rising dimensionless Weissenberg number from $We = 0.5$ to 4. Yellow color lines represent $We = 0.5$, blue lines for $We = 1$, green lines for $We = 3$, and brown lines for $We = 4$. Arrow direction points out that an increase in We decrease $f'(\eta)$ and fluid is approaching the vertical wall in a downward direction. (For interpretation of the references to color in this figure legend, the reader is referred to the Web version of this article.)

$$E_g = \frac{k_f}{T_\infty{}^2}\left[\left(\frac{\partial T}{\partial x}\right)^2 + \left(\frac{\partial T}{\partial y}\right)^2\right] + \frac{\mu_f}{T_\infty}\left(\frac{\partial u}{\partial y}\right)^2 + \frac{\sigma B^2 \sin^2(\omega) u^2}{T_\infty} + R\,\frac{D_B}{C_\infty}\left(\frac{\partial G_a}{\partial y}\right)^2 + R\,\frac{D_B}{T_\infty}\left(\frac{\partial T}{\partial y}\right)\left(\frac{\partial G_a}{\partial y}\right). \tag{20}$$

The first term indicates heat irreversibility, the second term is all about fluid friction, the third factor depicts magnetic field, the fourth points out mass transport and the last one is the combination of heat as well as mass transference phenomenon. The expression in the form of entropy generation is enumerated underneath

$$N_g = \frac{E_g}{k_f / x^2 \Omega_T^2}, \tag{21}$$

the dimensionless expression regarding entropy generation is bestowed by

$$N_g = N_{gh} + N_{gf} + N_{gM} + N_{gm} + N_{ghm}\,. \tag{22}$$

The expression $N_{gh}, N_{gf}, N_{gM}, N_{gm}, N_{ghm}$ in the beyond formula denotes the entropy generating due to heat transference, fluid friction, magnetic field, mass transfer, combined mass as well as heat transfer mathematically expressed below

$$\left.\begin{aligned} N_{gh} = \left(\frac{m+1}{2}\right) Re_x \theta'^{2'}, N_{gf} = \left(\frac{m+1}{2}\right)\left(\frac{Br}{\Omega_T}\right) Re_x f''^2, \\ N_{gM} = M\left(\frac{Br}{\Omega_T}\right) Re_x f'^2, N_{gm} = \left(\frac{m+1}{2}\right) M_m \left(\frac{\Omega_C}{\Omega_T}\right)^2 Re_x \vartheta'^2, \\ N_{ghm} = \left(\frac{m+1}{2}\right) M_m \left(\frac{\Omega_C}{\Omega_T}\right) Re_x \theta' \vartheta', \\ . \end{aligned}\right\} \tag{23}$$

whereas

$$\left.\begin{aligned} Br = \frac{\mu_f u_e^2}{k_f (T_w - T_\infty)}, Re_x = \frac{u_e x}{\nu_f}, \Omega_T = \frac{(T_w - T_\infty)}{T_\infty}, \\ \Omega_c = \frac{(C_w - C_\infty)}{C_\infty}, M_m = \frac{R D_B C_\infty}{k_f}. \end{aligned}\right\} \tag{24}$$

7. Result and discussion

This section is intended to study the effect of several dimensionless factors, like the Weissenberg number *We* and viscosity index *n* appear due to cross fluid, wedge parameter *m* (wedge geometry), Casson fluid parameter, and porosity parameter appear due to porous media. Thermal radiation parameter *Rd*, thermal conductivity, heat generation *Q*, Brownian diffusion *Nb*, homogeneous reaction, heterogeneous reaction, Schmidt number is *Sc*, Brinkman number is *Br*, and Reynolds's number is *Re* (due to entropy generation) on velocity, temperature, concentration, entropy fields, Bejan number, skin friction coefficient, and heat transfer Nusselt number. Obtained outcomes are portrayed in the form of figures and tables. A solid line in all figures indicates tetra-hybrid nanoparticles; a dashed

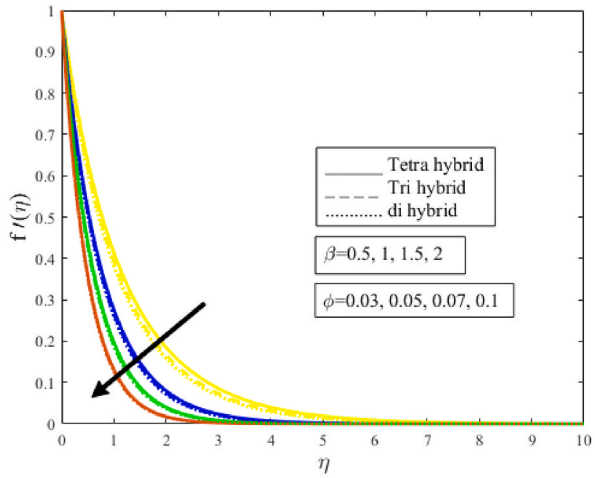

Fig. 3(b). Velocity profile $f'(\eta)$ decreases by rising dimensionless Casson fluid parameter β from $\beta = 0.5$ to 2. Yellow color lines represent $\beta = 0.5$, blue lines for $\beta = 1$, green lines for $\beta = 1.5$, and brown lines for $\beta = 2$. Arrow direction points out that an increase in β decrease $f'(\eta)$ and fluid is approaching the vertical wall in a downward direction. Symbol φ represents an increase in the volume fraction of nanoparticles. (For interpretation of the references to color in this figure legend, the reader is referred to the Web version of this article.)

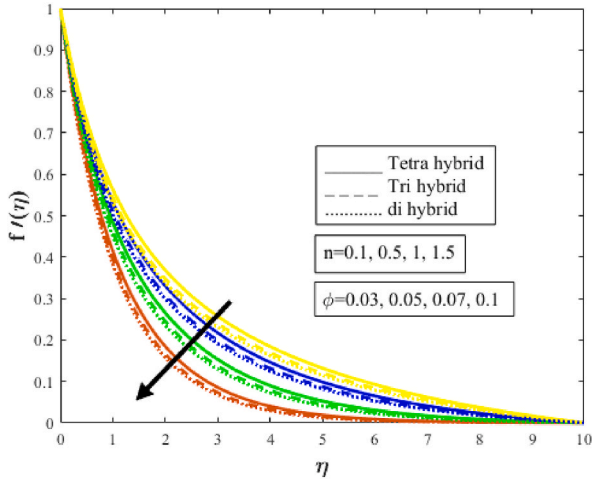

Fig. 3(c). Velocity profile $f'(\eta)$ decreases by rising dimensionless viscosity index parameter n from $n = 0.1$ to 1.5. Yellow color lines represent $n = 0.1$, blue lines for $n = 0.5$, green lines for $n = 1$, and brown lines for $n = 1.5$. Arrow direction points out that an increase in n decrease $f'(\eta)$ and fluid is approaching the vertical wall in a downward direction. Symbol φ represents an increase in the volume fraction of nanoparticles. (For interpretation of the references to color in this figure legend, the reader is referred to the Web version of this article.)

line indicates tri-hybrid nanoparticles; and a dotted line represents di-hybrid nanoparticles. The arrow in all figures indicates the fluid is approaching or moving away from the vertical wall by amplifying the value of various parameters. The volume fraction of nanoparticles is denoted by a symbol having values of 0.3, 0.05, 0.07, and 0.1, which represent 3%, 5%, 7%, and 10% of the solute (nanoparticles) in the solution termed as base fluid (ethanol).

7.1. Effect of sundry parameters on the velocity field

The time needed by liquid to rest is linked with the Weissenberg phenomenon. Viscosity diminishes under enrichment in *We* brings about a decrement in the velocity field. Because of a decreased shear viscosity, the average fluid velocity rises as the *We* rises as shown in Fig. 3(a). The behavior of Casson fluid parameter *M* is similar to Casson fluid parameter β on $f'(\eta)$ is highlighted in Fig. 3(b). The fluid becomes thick for $\beta < 0$, $\beta = 0$ Newtonian fluid in addition to shear thickening for $\beta > 0$. Casson Sutterby fluid is a viscoelastic fluid having viscosity changes over time. Daily life products having viscosity changes over time are ketchup, paint, blood, spaghetti, polymers, etc. The fluid becomes thick by amplifying TETHNF seen in Fig. 3(b). Fig. 3(c) is designed to investigate the performance of n against $f'(\eta)$. Symbol n tells us about the viscous nature of the liquid. Viscosity amplifies for $n > 1$, Newtonian $n = 1$, diminishes in the case of $n < 1$. Viscosity topples the inertia element of liquid by rising n which reduces $f'(\eta)$. The effect of porosity parameter λ on $f'(\eta)$ is highlighted in Fig. 3(d). The porosity phenomenon is linked with Darcian law. According to Darcian theory, the change in pressure and

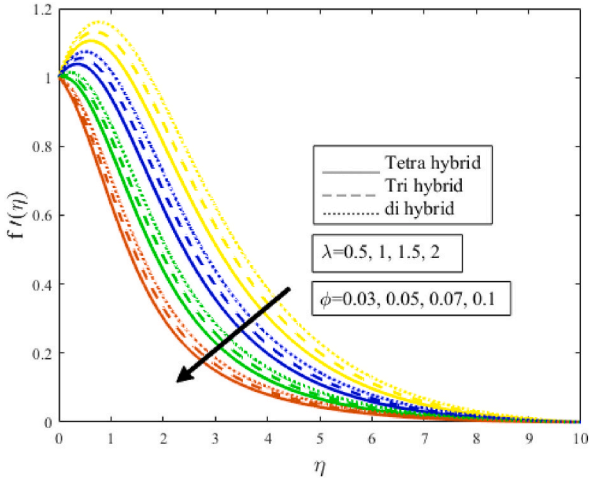

Fig. 3(d). Velocity profile $f'(\eta)$ decreases by rising dimensionless porosity parameter λ from $\lambda = 0.5$ to 2. Yellow color lines represent $\lambda = 0.5$, blue lines for $\lambda = 1$, green lines for $\lambda = 1.5$, and brown lines for $\lambda = 2$. Arrow direction points out that an increase in λ decrease $f'(\eta)$ and fluid is approaching the vertical wall in a downward direction. Symbol φ represents an increase in the volume fraction of nanoparticles. (For interpretation of the references to color in this figure legend, the reader is referred to the Web version of this article.)

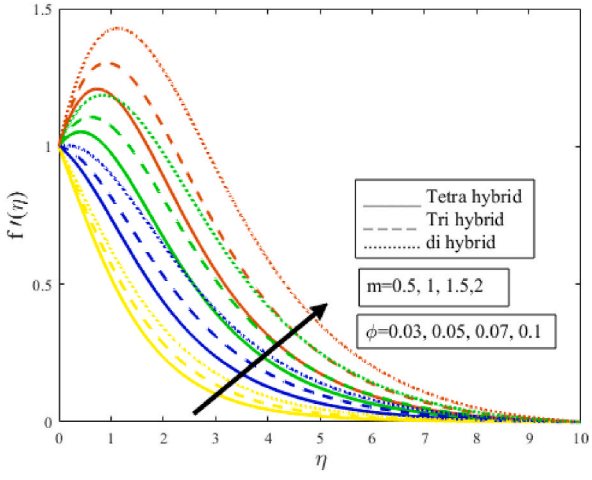

Fig. 3(e). Velocity profile $f'(\eta)$ increases by rising dimensionless wedge parameter m from $m = 0.5$ to 2. Yellow color lines represent $m = 0.5$, blue lines for $m = 1$, green lines for $m = 1.5$, and brown lines for $m = 2$. Arrow direction points out that an increase in m amplifies $f'(\eta)$ and fluid is moving away from the vertical wall in an upward direction. Symbol φ represents an increase in the volume fraction of nanoparticles. (For interpretation of the references to color in this figure legend, the reader is referred to the Web version of this article.)

velocity of liquid are directly related. Darcian body force is opposite to the permeability of the fluid flow medium, so it brings about a deceleration in a fluid motion. A change in pressure amplifies density as well as resistance. Fluid is not moving easily through the porous medium and approaches the vertical wall as shown in Fig. 3(d). From Fig. 3(e) it is observed that $f'(\eta)$ amplifies by magnifying wedge parameter m provides a hurdle to fluid movement in addition amplifies $f'(\eta)$..

7.2. Impact of distinguished parameters on temperature field

Fig. 4(a) reflects the radiation parameter *Rd* impact on $\theta(\eta)$. Thermal radiation is put in use in situations that call for a significant temperature difference and has enormous utilization in nuclear reactors as well as burning reactors. Manufacturing polymers, cleaning water, and other similar activities. Magnification of *Rd* causes a greater degree of randomness in the collisions between molecules. The enhancement of *Rd* phenomena caused by the implantation of tetra nanocomposites into the base liquid results in an increase in both $\theta(\eta)$ and the width of a thermal boundary layer. The radiation effect amplifies in the occurrence of TETHNF other than THNF and HNF. Fig. 4(b) reflects the impact of thermal conductance ε on $\theta(\eta)$. Thermal conductivity is the ability of a material to conduct heat. It is well established that in liquids thermal conductivity amplifies as a result of the collision of fluid atoms. Molecules of the fluid share more kinetic energy with each other. It is well established that TBL layer thickness amplifies more for TETHNF in contrast to TEHNF as shown in the figure. The stretching sheet distributes incremental heat by amplifying ε which improves heat distribution in the system.

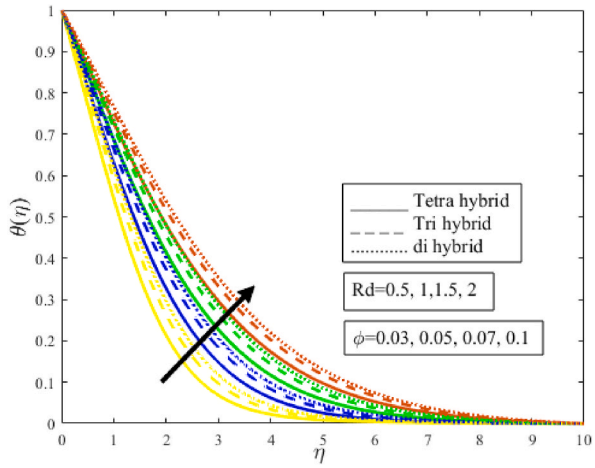

Fig. 4(a). Temperature profile $\theta(\eta)$ augments by rising dimensionless radiation parameter Rd from $Rd = 0.5$ to 2. Yellow color lines represent $Rd = 0.5$, blue lines for $Rd = 1$, green lines for $Rd = 1.5$, and brown lines for $Rd = 2$. Arrow direction points out that an increase in Rd amplifies $\theta(\eta)$ and fluid is flowing away from the vertical wall in an upward direction. Symbol φ represents an increase in the volume fraction of nanoparticles. (For interpretation of the references to color in this figure legend, the reader is referred to the Web version of this article.)

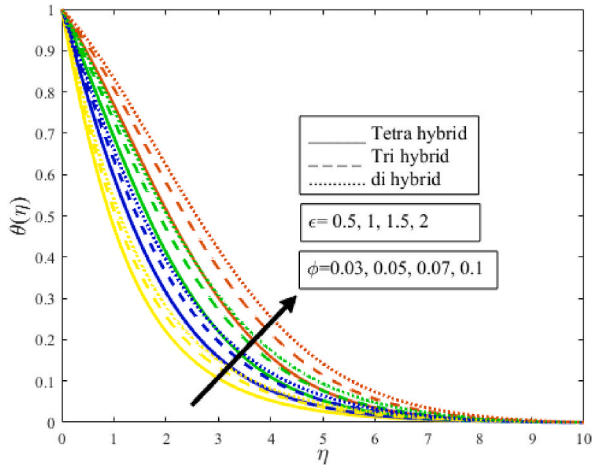

Fig. 4(b). Temperature profile $\theta(\eta)$ augments by rising dimensionless thermal conductivity parameter ε from $\varepsilon = 0.5$ to 2. Yellow color lines represent $\varepsilon = 0.5$, blue lines for $\varepsilon = 1$, green lines for $\varepsilon = 1.5$, and brown lines for $\varepsilon = 2$. Arrow direction points out that an increase in ε amplifies $\theta(\eta)$ and fluid is moving away from the vertical wall in an upward direction. Symbol φ represents an increase in the volume fraction of nanoparticles. (For interpretation of the references to color in this figure legend, the reader is referred to the Web version of this article.)

Parameter Q influence on $\theta(\eta)$ is highlighted in Fig. 4(c). It is quite evident that more heat is absorbed by the fluid as a result elevates Q and thermal boundary thickness in addition $\theta(\eta)$. TETHNF delivers more heat rather than THNF and HNF.

7.3. Influence of distinguished parameters on concentration

Fig. 5(a) displayed the impact of Ks on $\varphi(\eta)$. Diffusivity and concentration are directly linked with each other. In the case of a homogeneous reaction both liquid and catalyst are in the same phase which is also one of the prominent factors for an augmentation in the concentration field. The flow diffusivity also fluctuates by raising the value of the homogeneous reaction, which lessens $\varphi(\eta)$. With a greater proportion of chemical organisms participating throughout the chemical process just at the biochemical frontline, the concentration of something like the reactive species increases even the speed at which the velocity of such a heterogeneous reaction increase. As can be shown in Fig. 5(b), the change in concentration is affected by K_2. The change in concentration is amplified when K_2 is raised. Increases mostly in the rate of a homogeneous reaction mechanism led to a steeper change in concentration $\varphi(\eta)$ because more organisms are being utilized. In the case of fixed molecular diffusion, when Sc amplifies, the viscous diffusion also amplifies. Schmidt number is directly related to the diffusion phenomenon and performs the same role for the concentration equation as the Prandtl number for the energy equation. Schmidt number is related to molecular diffusivity. It is quite clear that an incremental change in molecular diffusivity enhances fluid concentration. The concentration of the fluid increases under amplification in Sc which increases $\varphi(\eta)$ as shown in Fig. 5(c).

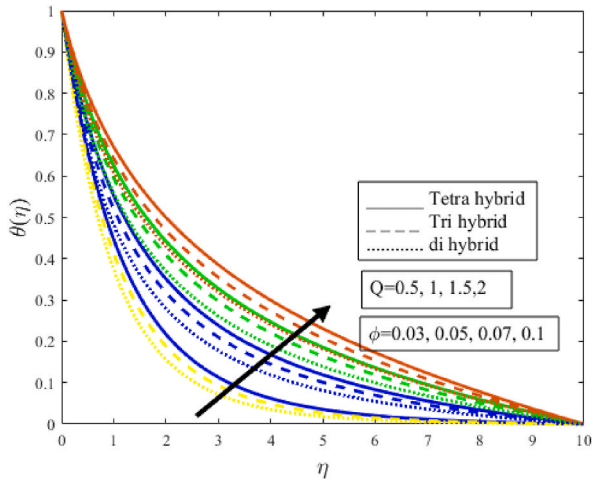

Fig. 4(c). Temperature profile $\theta(\eta)$ augments by rising dimensionless heat generation parameter Q from $Q = 0.5$ to 2. Yellow color lines represent $Q = 0.5$, blue lines for $Q = 1$, green lines for $Q = 1.5$, and brown lines for $Q = 2$. Arrow direction points out that an increase in Q amplifies $\theta(\eta)$ and fluid is moving away from the vertical wall in an upward direction. Symbol φ represents an increase in the volume fraction of nanoparticles. (For interpretation of the references to color in this figure legend, the reader is referred to the Web version of this article.)

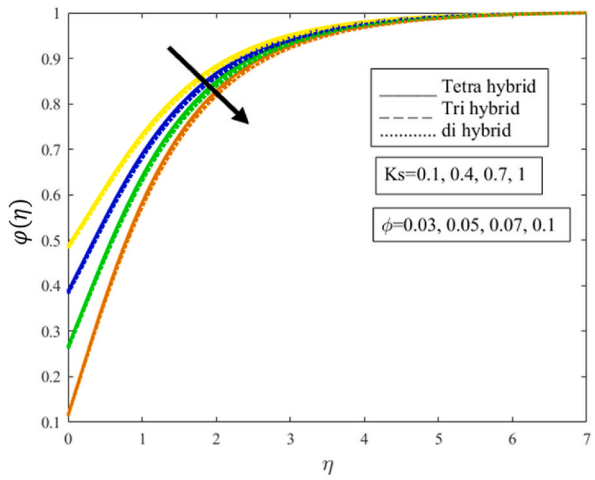

Fig. 5(a). Concentration profile $\varphi(\eta)$ diminishes by rising dimensionless heterogeneous reaction parameter K_s from $K_s = 0.1$ to 1. Yellow color lines represent $K_s = 0.1$, blue lines for $K_s = 0.4$, green lines for $K_s = 0.7$, and brown lines for $K_s = 1$. Arrow direction points out that an increase in K_s diminishes $\varphi(\eta)$ and fluid is approaching the vertical wall in a downward direction. Symbol φ represents an increase in the volume fraction of nanoparticles. (For interpretation of the references to color in this figure legend, the reader is referred to the Web version of this article.)

7.4. Effect of dimensionless parameters on entropy generation

Fig. 6(a and b) show the effect of *Br* and *Re* on the entropy generation *Ng*. When *Br* is raised, the system's physical parameters alter in such a way that the conduction frequency of heat that is created as a result of viscous dissipation is lowered. This occurs because the conduction frequency of heat increases as the temperature of the system rises. This results in an increase in the rate at which entropy is produced. Increasing *Re* causes a shift in the behavior of the fluid, which transitions from laminar to turbulent. This is because the heat dissipation phenomenon is amplified by soaring *Re*, which accentuates *Ng*. The primary focus of attention in Fig. 6(c) is placed on the entropy-generating process known as *Ng*, which occurs as a consequence of a positive shift in *We*. It is very much clear that relaxation time for liquid by improving *We* which in turn amplifies the viscosity of the fluid flow and diminishes momentum boundary layer width and entropy generation *Ng*. The influence that *Br* and *Re* have on the Bejan number is shown in Fig. 6(d and e), which you can see here. Both entropy creation and having characteristics that are opposed to one another. *Ng* is amplified, whereas *Be* is diminished when there is a positive fluctuation in *Br* and *Re*.

Another important key aspect of physical quantities local skin friction coefficient and Nusselt number with various parameters are seen through tables. The physical quantity of skin friction is the friction force of fluid against the surface of an object that is moving on the surface. In fluid analysis, it is friction between the fluid and the surface on which the fluid is flowing. On the other hand, the heat transfer rate of fluid, when it moves on a solid body, is inspected by the Nusselt number. The attitude of both said quantities are shown

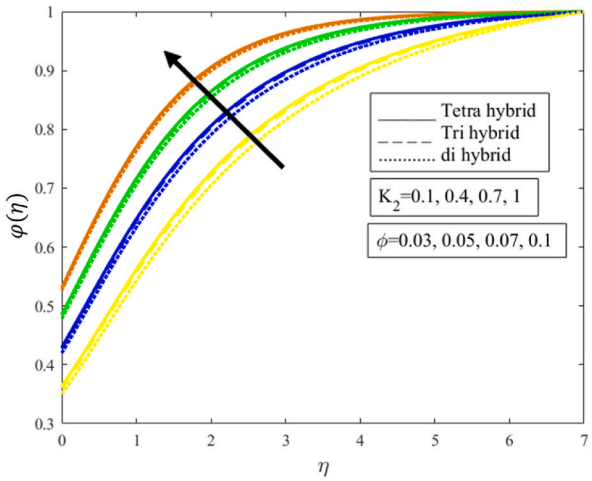

Fig. 5(b). Concentration profile $\varphi(\eta)$ augments by rising dimensionless homogeneous reaction parameter K_2 from $K_2 = 0.1$ to 1. Yellow color lines represent $K_2 = 0.1$, blue lines for $K_2 = 0.4$, green lines for $K_2 = 0.7$, and brown lines for $K_2 = 1$. Arrow direction points out that an increase in K_2 amplifies $\varphi(\eta)$ and fluid is moving away from the wall in an upward direction. Symbol φ represents an increase in the volume fraction of nanoparticles. (For interpretation of the references to color in this figure legend, the reader is referred to the Web version of this article.)

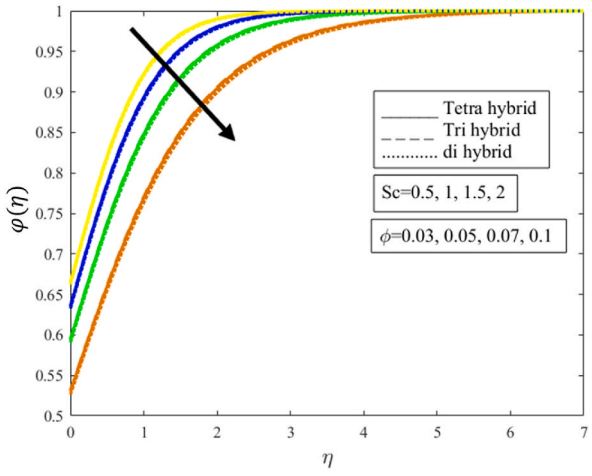

Fig. 5(c). Concentration profile $\varphi(\eta)$ diminishes by rising dimensionless Schmidt number Sc from $Sc = 0.5$ to 2. Yellow color lines represent $Sc = 0.5$, blue lines for $Sc = 1$, green lines for $Sc = 1.5$, and brown lines for $Sc = 2$. Arrow direction points out that an increase in Sc decreases $\varphi(\eta)$ and fluid is approaching the vertical wall in a downward direction. Symbol φ represents an increase in the volume fraction of nanoparticles. (For interpretation of the references to color in this figure legend, the reader is referred to the Web version of this article.)

in Table 4. From Table 4 heat transference rate amplifies more for TETHNF than HNF. Relative percentage error is maximum for $Rd = 2$ and minimum for $\varepsilon = 1$. Table 5 reflects sundry parameters' influence on the drag phenomenon and heat transfer rate. It is observed that magnification in *We*, *n*, β, λ, *Pr*, *Rd*, *M*, and *Q* brings about a decrement in drag coefficient and a positive variation in *Ks* amplifies drag friction phenomenon. Substantial progress in β, *Pr*, *Rd*, ε, *Ks*, *M* also *Q* brings about an increment in heat transport rate but opposite behavior for *We*, *n*, and λ.

8. Statistical analysis of sundry parameters on skin friction coefficient and Nusselt number

The effect of *n* on the drag coefficient of either surface is shown in Fig. 7(a). Improvements in stickiness will *n* slow down the liquid significantly. Reduced *n* makes this skin friction even more pronounced, increasing the drag resistance of a layer where the liquid is traveling. Contact at the layer is what practically slows down the fluid's rate of travel. As n increases, the thickness of either the liquid increases, slowing the overall flow and therefore increasing the drag close to the surface. Fig. 7(b) provides the impact of β on the drag coefficient. Surface drag is the velocity of fluid flow against the medium velocity. It is noticed that fluid velocity diminishes by rising β which depreciates the surface drag phenomenon. Physically viscous forces dominate inertial forces which diminishes liquid rapidity, in addition to the drag friction effect. The influence of the Weissenberg number on surface drag friction is highlighted in Fig. 7(c). Weissenberg's number is related to relaxation time. During that time the viscosity of fluid amplifies, and fluid is unable to move easily

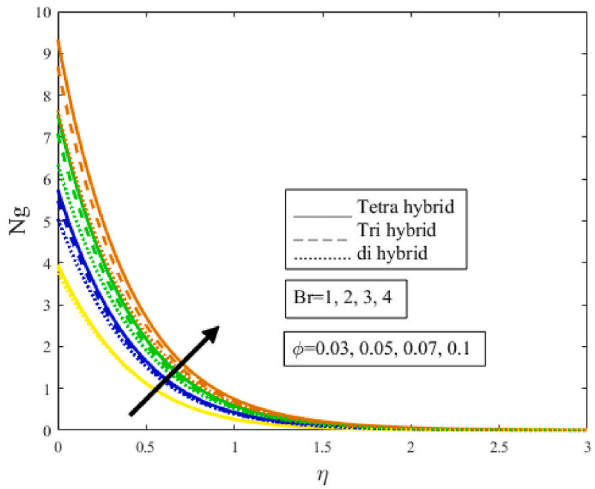

Fig. 6(a). Entropy generation profile *Ng* augments by rising dimensionless Brinkman number *Br* from $Br = 1$ to 4. Yellow color lines represent $Br = 0.1$, blue lines for $Br = 2$, green lines for $Br = 3$, and brown lines for $Br = 4$. Arrow direction points out that an increase in *Br* amplifies *Ng* and fluid is moving away from the vertical wall in an upward direction. Symbol φ represents an increase in the volume fraction of nanoparticles. (For interpretation of the references to color in this figure legend, the reader is referred to the Web version of this article.)

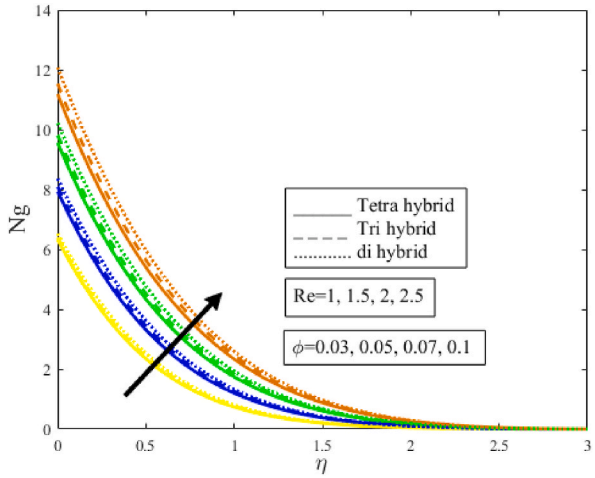

Fig. 6(b). Entropy generation profile *Ng* augments by rising dimensionless Reynolds number *Re* from $Re = 1$ to 2.5. Yellow color lines represent $Re = 1$, blue lines for $Re = 1.5$, green lines for $Re = 2$, and brown lines for $Re = 2.5$. Arrow direction points out that an increase in *Re* amplifies *Ng* and fluid is moving away from the vertical wall in an upward direction. Symbol φ represents an increase in the volume fraction of nanoparticles. (For interpretation of the references to color in this figure legend, the reader is referred to the Web version of this article.)

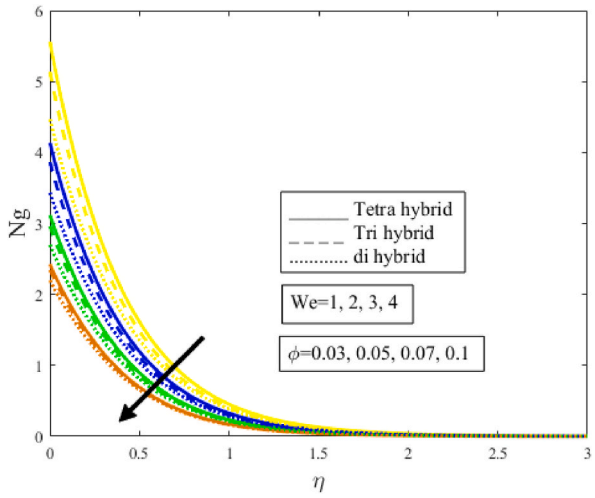

Fig. 6(c). Entropy generation profile *Ng* diminishes by rising dimensionless Weissenberg number *We* from $We = 1$ to 4. Yellow color lines represent $We = 1$, blue lines for $We = 2$, green lines for $We = 3$, and brown lines for $We = 4$. Arrow direction points out that an increase in Re depreciates *Ng* and fluid is approaching the vertical wall in a downward direction. Symbol φ represents an increase in the volume fraction of nanoparticles. (For interpretation of the references to color in this figure legend, the reader is referred to the Web version of this article.)

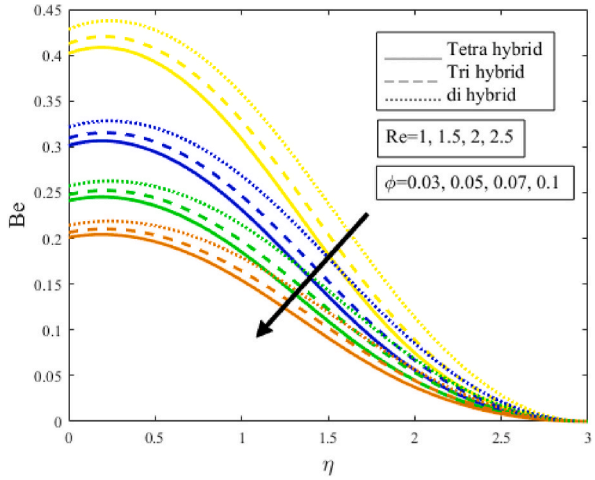

Fig. 6(d). Bejan number *Be* diminishes by rising dimensionless Reynold's number *Re* from $Re = 1$ to 2.5. Yellow color lines represent $Re = 1$, blue lines for $Re = 1.5$, green lines for $Re = 2$, and brown lines for $Re = 2.5$. Arrow direction points out that an increase in *Re* depreciates *Be* and fluid is approaching the vertical wall in a downward direction. Symbol φ represents an increase in the volume fraction of nanoparticles. (For interpretation of the references to color in this figure legend, the reader is referred to the Web version of this article.)

over the expandable sheet. The velocity depreciates by improving *We*. Drag friction is the friction caused against the medium layer. Liquid rapidity diminishes by magnifying *We* which amplifies drag friction mentioned in Fig. 7(d). The internal temperature of a fluid decreases with nothing but an increase in *Pr*. A larger *Pr* allows for faster heat diffusion, resulting in lower liquid temperatures and even a lower Nusselt number for heat transmission, as seen in Fig. 7(e). The radiation parameter *Rd* is an important aspect to amplify heat transport having immense applications in thermal enhancement, which is further utilized in combustion reactors, paper production, polymer production, etc. Thermal conductivity amplifies in the presence of *Rd* improves liquid temperature and including nanoparticles amplifies *Rd* phenomenon and heat transfer phenomenon sketched in Fig. 7(e).

9. Conclusion

The present study is designed to investigate the impact of homogeneous/heterogeneous chemical reactions on a cross nanofluid past a wedge accompanied by an inclined magnetic field and heat generation effect. The article is novel in the sense that the effect of homogeneous/heterogeneous in the case of any non-Newtonian fluid past a wedge never have been explored in the existing literature. The present study is molded in the context of nanoparticles' impact on ethanol biofuel. The bvp4c numerical technique is used to obtain the numerical solution of the proposed model. Some important conclusive remarks are mentioned underneath.

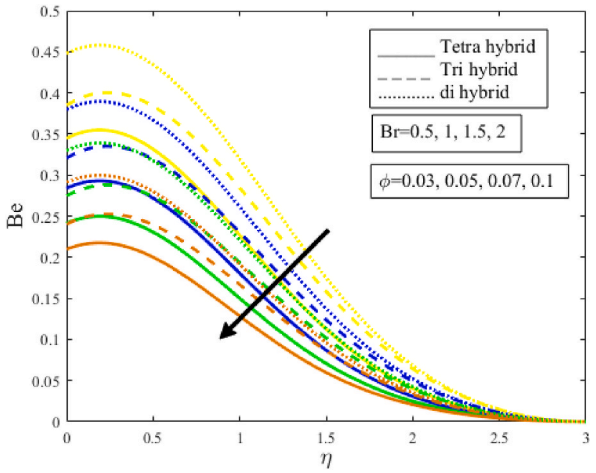

Fig. 6(e). Bejan number *Be* diminishes by rising dimensionless Brinkman number *Br* from $Br = 0.5$ to 2. Yellow color lines represent $Br = 0.5$, blue lines for $Br = 1$, green lines for $Br = 1.5$, and brown lines for $Br = 2$. Arrow direction points out that an increase in *Br* depreciates *Be* and fluid is approaching the vertical wall in a downward direction. Symbol φ represents an increase in the volume fraction of nanoparticles. (For interpretation of the references to color in this figure legend, the reader is referred to the Web version of this article.)

Table 4
Measure of frictional force versus certain factors.

ε	Pr	Q	Rd	$\frac{-1}{Nu_x Re_x^{2}}$ Tetra nanoparticles	$\frac{-1}{Nu_x Re_x^{2}}$ Ternary nanoparticles	Relative % $\frac{Nu_{tethnf} - Nu_{thnf}}{Nu_{tethnf}}$%
0.5	40	0.1	0.5	1.5125	1.2386	12.5 %
0.7				1.6875	1.4412	10.4 %
0.9				1.7018	1.5753	9.1 %
1.0				1.9579	1.7215	8.7 %
	41			1.7176	1.4321	12.2 %
	42			2.0213	1.8041	12.3 %
	43			2.2967	2.0651	11.5 %
		0.3		1.6178	1.4298	11.6 %
		0.5		1.8458	1.6176	11.4 %
		0.7		2.1475	1.8815	4.62 %
			1	2.0567	1.6765	13.3 %
			1.5	2.1487	1.8521	13.6 %
			2	2.3346	2.0331	14.8 %

i. Relaxation time of the fluid magnifies because of an incremental change in the Weissenberg number which diminishes the velocity phenomenon and the drag friction coefficient.
ii. A positive change in inclination angle strengthens viscous forces in contrast to inertial forces providing a decrement in fluid velocity.
iii. Catalytic chemical reactions amplify by amplifying Q, k_2 which empowers the fermentation process during ethanol production.
iv. Lorentz force which is a resistive force generated when electrically conducting liquid moving through a magnetic field amplifies viscosity and elevates temperature.
v. TETHNF delivers more heat rather than THNF and HNF.
vi. Fermentation time during ethanol production decreases because of the inclusion of TETHNF in ethanol.
vii. Substantial change in thermal radiation *Rd* and variable thermal conductivity ε provide extensive heat which is used during the process of saccharification and fermentation to achieve a large amount of ethanol.
viii. It is observed that magnification in homogeneous/heterogeneous catalytic chemical reaction speed up the fermentation reaction rate and generates more which contributes a lot to ethanol production.
ix. Through the incorporation of TETHNF, a diesel automobile engine running on ethanol gasoline may efficiently function, providing significant enhancement and successfully controlling pollutants.
x. Magnification in Reynolds number *Re* and Brinkman number amplifies the overall entropy of the system but diminishes Bejan number.
xi. Amplification in heat generation parameter Q delivers more heat to a fluid which amplifies the heat transfer rate and elevates the fermentation process of the waste material.

Table 5
Description of sundry parameters on surface drag coefficient and heat transfer rate.

We	*n*	*β*	*λ*	*Pr*	*Rd*	*ε*	*Q*	*Ks*	*M*	Skin friction	Nusselt number
0.1	0.1	1.0	0.1	40	0.1	0.1	0.1	1.0	0.1	1.7742	0.3156
0.5										1.7630	0.3015
1.0										1.7598	0.2960
	0.3									1.3295	0.2425
	0.5									1.2833	0.2015
	0.7									1.2624	0.1186
		1.5								1.4145	0.2535
		2								1.3926	0.3056
		2.5								1.3752	0.3327
			0.03							1.4143	0.8748
			0.05							1.4036	0.4820
			0.07							1.3930	0.3150
				41						1.3386	0.7631
				42						1.3252	1.3247
				43						1.3117	1.8773
					0.2					1.3415	0.9736
					0.3					1.3207	1.5768
					0.4					1.3196	1.9217
						0.3				1.3445	1.0156
						0.5				1.2385	1.3216
						0.7				1.1572	1.5763
							0.4			1.3845	0.6213
							0.7			1.3021	0.8751
							0.9			1.2539	0.4320
								1.5		1.3758	0.4610
								2.0		1.4021	0.5321
								2.5		1.4291	0.6931
									0.5	1.3125	0.7953
									1	1.1957	0.8271
									1.5	1.1176	0.9155

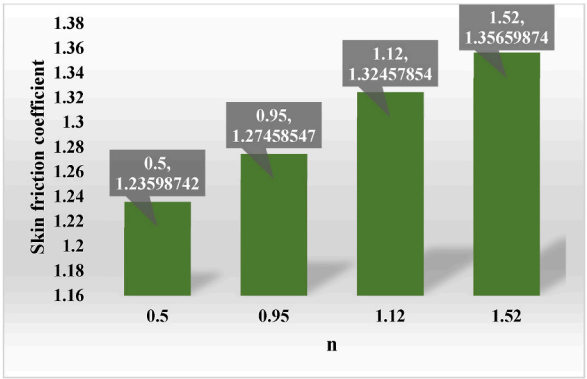

Fig. 7(a). Skin friction coefficient (vertical) augments by rising viscosity index parameter n (horizontal) from $n = 0.5$ to 1.52. Green vertical bars represent the skin friction coefficient increasing vertically from 1.23598742 to 1.35659874 by amplifying n from 0.5 to 1.52. (For interpretation of the references to color in this figure legend, the reader is referred to the Web version of this article.)

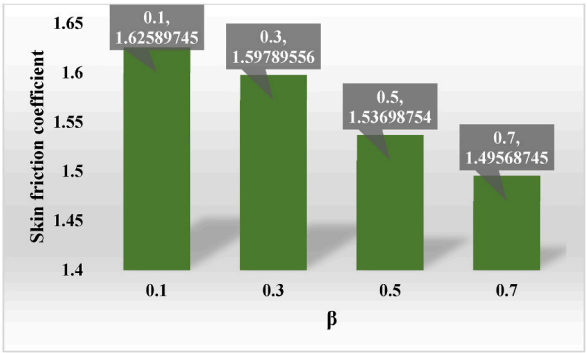

Fig. 7(b). Skin friction coefficient (vertical) diminishes by rising Casson fluid parameter β (horizontal) from $\beta = 0.1$ to 0.7. Green vertical bars represent the skin friction coefficient depreciating vertically from 1.62589745 to 1.49568745 by amplifying β from 0.1 to 0.7. (For interpretation of the references to color in this figure legend, the reader is referred to the Web version of this article.)

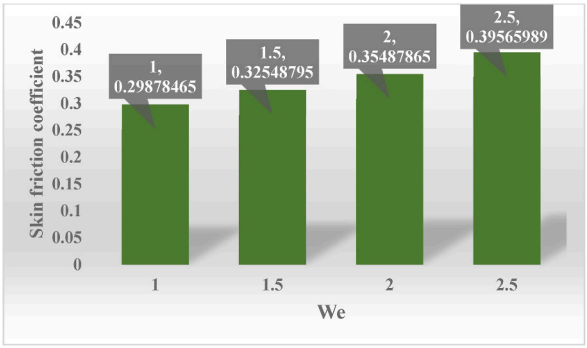

Fig. 7(c). Skin friction coefficient (vertical) augments by rising Weissenberg number *We* (horizontal) from $We = 1$ to 2.5. Green vertical bars represent the skin friction coefficient increasing vertically from 0.29878465 to 0.39565989 by amplifying *We* from 1 to 2.5. (For interpretation of the references to color in this figure legend, the reader is referred to the Web version of this article.)

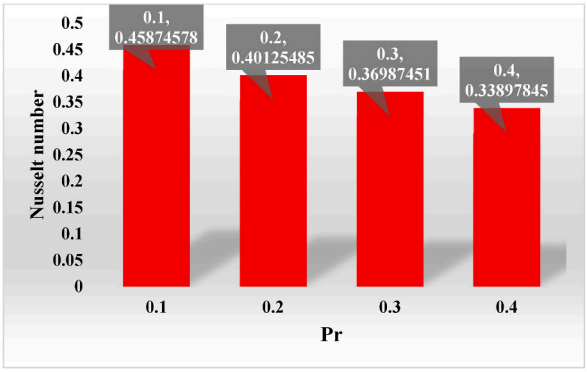

Fig. 7(d). Heat transfer Nusselt number (vertical) diminishes by rising Prandtl number *Pr* (horizontal) from $Pr = 0.1$ to 0.4. Red vertical bars represent heat transfer Nusselt number depreciates vertically from 0.45874578 to 0.33897845 by amplifying *Pr* from 0.1 to 0.4. (For interpretation of the references to color in this figure legend, the reader is referred to the Web version of this article.)

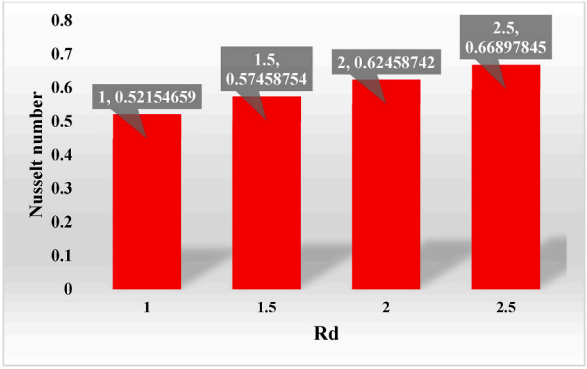

Fig. 7(e). Heat transfer Nusselt number (vertical) augments by rising radiative parameter *Rd* (horizontal) from $Rd = 1$ to 2.5. Red vertical bars represent heat transfer Nusselt number amplifies vertically from 0.52154659 to 0.66897845 by amplifying *Rd* from 1 to 2.5. (For interpretation of the references to color in this figure legend, the reader is referred to the Web version of this article.)

Credit author statement

Tanveer Sajid and Wasim Jamshed formulated the problem. Wasim Jamshed and Mohamed R. Eid solved the problem. Tanveer Sajid, Abdullatif A. Gari, Wasim Jamshed, Mohamed R. Eid, Nazrul Islam, Kashif Irshad, Gilder Cieza Altamirano and Sayed M El Din, computed and scrutinized the results. All the authors equally contributed in writing and proof reading of the paper. All authors reviewed the manuscript.

Declaration of competing interest

The authors declare that they have no known competing financial interests or personal relationships that could have appeared to influence the work reported in this paper.

Data availability

Data will be made available on request.

Acknowledgments

This research work was funded by Institutional Fund Projects under grant no. (**IFPIP**: 1312–135–1443). The authors gratefully acknowledge the technical and financial support provided by the Ministry of Education and King Abdulaziz University, DSR, Jeddah, Saudi Arabia.

Nomenclature

M	Magnetic effect
Pr	Prandtl number
λ	Porosity
F_w	Suction/injection parameter
ε_1	Stretching/shrinking wedge parameter
K_2	Strength of homogeneous reaction
K_1	Rate coefficient of homogeneous reaction
τ	specific heat at constant pressure to specific heat of fluid
We	Weissenberg number
Rd	Thermal radiation
Nu_x	Nusselt number
τ_w	Wall shear stress
q_m	Wall mass flux
Re	Reynolds number
n	Power index
m	Wedge parameter
ε	Thermal conductivity
Sc	Schmidt number
D_A, D_B	Diffusion of chemical species
C_p	Capacity of the heat

β	Casson fluid parameter
$k(T)$	thermal conductivity
C	Concentration
ω	Inclination in angle
Cf_x	Skin friction
q_w	Wall heat flux
Br	Brinkman number
φ	Concentration field

References

[1] S.U.S. Choi, Enhancing thermal conductivity of fluids with nanoparticles, ASME-Publications-Fed 231 (1995) 99–106.
[2] S. Lee, S.U.S. Choi, S. Li, J.A. Eastman, Measuring thermal conductivity of fluids containing oxide nanoparticles, J. Heat Tran. 121 (1999) 280–289.
[3] J. Buongiorno, Convective transport in nanofluids, J. Heat Tran. 128 (2006) 240–250.
[4] I.D. Boyd, M.J. Martin, Falkner-Skan flow over a wedge with slip boundary conditions, J. Thermophys. Heat Tran. 24 (2) (2010) 263–270.
[5] W.A. Khan, I. Pop, Boundary-layer flow of a nanofluid past a stretching sheet, Int. J. Heat Mass Tran. 53 (2010) 2477–2483.
[6] M. Sheikholeslami, M.G. Bandpy, D.D. Ganji, Numerical investigation of MHD effect on Al2O3- nanofluid flow and heat transfer in a semi-annulus enclosure using LBM, Energy 1 (60) (2013) 501–510.
[7] W.N. Mutuku-Njane, O.D. Makinde, On hydromagnetic boundary layer flow of nanofluids over a permeable moving surface with Newtonian heating, Lat. Am. Appl. Res. 44 (2014) 57–62.
[8] F. Mabood, W.A. Khan, A.I.M. Ismail, MHD boundary layer flow and heat transfer of nanofluids over a nonlinear stretching sheet: a numerical study, J. Magn. Magn Mater. 374 (2015) 569–576.
[9] M. Khan, A.A. Hafeez, A review on slip-flow and heat transfer performance of nanofluids from a permeable shrinking surface with thermal radiation: dual solutions, Chem. Eng. Sci. 173 (2017) 1–11.
[10] M. Khan, A.A. Hafeez, A review on slip-flow and heat transfer performance of nanofluids from a permeable shrinking surface with thermal radiation: dual solutions, Chem. Eng. Sci. 173 (2017) 1–11.
[11] Y. Ma, R. Mohebbi, M.M. Rashidi, Z. Yang, MHD convective heat transfer of Ag–Mg/water hybrid nanofluid in a channel with active heaters and coolers, Int. J. Heat Mass Tran. 137 (2019) 714–726.
[12] A. Hamid, M.K. Hashim, M. Alghamd, MHD Blasius flow of radiative Williamson nanofluid over a vertical plate, Int. J. Mod. Phys. B 33 (2019), 1950245.
[13] B. Mahanthesh, Flow and heat transport of nanomaterial with quadratic radiative heat flux and aggregation kinematics of nanoparticles, Int. Commun. Heat Mass Tran. 127 (2021), 105521.
[14] M. Khan, M. Irfan, W.A. Khan, Impact of nonlinear thermal radiation and gyrotactic microorganisms on the Magneto-Burgers nanofluid, Int. J. Mech. Sci. 130 (2017) 375–382.
[15] M. Irfan, M. Khan, W.A. Khan, Impact of homogeneous–heterogeneous reactions and non-Fourier heat flux theory in Oldroyd-B fluid with variable conductivity, J. Braz. Soc. Mech. Sci. Eng. 41 (2019) 135.
[16] Adun Humphrey, Doga Kavaz, Mustafa Dagbasi, Review of ternary hybrid nanofluid: synthesis, stability, thermophysical properties, heat transfer applications, and environmental effects, J. Clean. Prod. 328 (2021), 129525.
[17] K.N. Sneha, G.P. Vanitha, U.S. Mahabaleshwar, D. Laroze, Effect of couple stress and mass transpiration on ternary hybrid nanoliquid over a stretching/shrinking sheet with heat transfer, Micromachines 13 (2022) 1694.
[18] J Suresh Goud, Pudhari Srilatha, R.S. Varun Kumar, K. Thanesh Kumar, Umair Khan, Zehba Raizah, Harjot Singh Gill, Ahmed M. Galal, Role of ternary hybrid nanofluid in the thermal distribution of a dovetail fin with the internal generation of heat, Case Stud. Therm. Eng. 35 (2022), 102113.
[19] S. Nasir, S. Sirisubtawee, P. Juntharee, et al., Heat transport study of ternary hybrid nanofluid flow under magnetic dipole together with nonlinear thermal radiation, Appl. Nanosci. 12 (2022) 2777–2788.
[20] Wenhao Cao, I.L. Animasaun, Se-Jin Yook, V.A. Oladipupo, Xianjun Ji, Simulation of the dynamics of colloidal mixture of water with various nanoparticles at different levels of partial slip: ternary-hybrid nanofluid, Int. Commun. Heat Mass Tran. 135 (2022), 106069.
[21] Z. Mahmood, Z. Iqbal, M.A. Alyami, B. Alqahtani, M.F. Yassen, U. Khan, Influence of suction and heat source on MHD stagnation point flow of ternary hybrid nanofluid over convectively heated stretching/shrinking cylinder, Adv. Mech. Eng. 19 (9) (2022).
[22] S.G. Krishna, M. Shanmugapriya, R. Sundareswaran, et al., MANFIS approach for predicting heat and mass transport of bio-magnetic ternary hybrid nanofluid using Cu/Al_2O_3/MWCNT nanoadditives, Biomass Conv. Bioref. (2022). In press. doi:10.1007/s13399-022-02989-x.
[23] T. Sajid, A. Ayub, S.Z.H. Shah, W. Jamshed, M.R. Eid, E.S.M.T. El Din, R. Irfan, S.M. Hussain, Trace of chemical reactions accompanied with arrhenius energy on ternary hybridity nanofluid past a wedge, Symmetry 14 (2022) 1850.
[24] Tanveer Sajid, Wasim Jamshed, Mohamed R. Eid, Gilder Cieza Altamirano, Farheen Aslam, Agaeb Mahal Alanzi, Assmaa Abd-Elmonem, Magnetized Cross tetra hybrid nanofluid passed a stenosed artery with nonuniform heat source (sink) and thermal radiation: novel tetra hybrid Tiwari and Das nanofluid model, J. Magn. Magn Mater. 569 (2023), 170443.
[25] T. Sajid, W. Jamshed, R.W. Ibrahim, M.R. Eid, A. Abd-Elmonem, M. Arshad, Quadratic regression analysis for nonlinear heat source/sink and mathematical Fourier heat law influences on Reiner-Philippoff hybrid nanofluid flow applying Galerkin finite element method, J. Magn. Magn Mater. 568 (2023), 170383.
[26] H. Guan, Q. Su, R. Wang, L. Huang, C. Shao, Z. Zhu, Why can hybrid nanofluid improve thermal conductivity more? A molecular dynamics simulation, J. Mol. Liq. 372 (2023), 121178.
[27] R. Wang, T. Chen, J. Qi, J. Du, G. Pan, L. Huang, Investigation on the heat transfer enhancement by nanofluid under electric field considering electrophoretic and thermophoretic effect, Case Stud. Therm. Eng. 28 (2021), 101498.
[28] J. Du, R. Wang, Q. Zhuo, W. Yuan, Heat transfer enhancement of Fe_3O_4-water nanofluid by the thermo-magnetic convection and thermophorestic effect, Int. J. Energy Res. 46 (7) (2022) 9521–9532.
[29] G. Wang, Z. Zhang, R. Wang, Z. Zhu, A review on heat transfer of nanofluids by applied electric field or magnetic field, Nanomaterials 10 (2020) 2386.
[30] A. Gailitis, On the possibility to reduce the hydrodynamic drag of a plate in an electrolyte, Appl. Magnetohydrodynam. Rep. Inst. Phys. Riga 13 (1961) 143–146.
[31] S. Abdal, I. Siddique, A.S. Alshomrani, F. Jarad, I.S.U. Din, S. Afzal, Significance of chemical reaction with activation energy for Riga wedge flow of tangent hyperbolic nanofluid in existence of heat source, Case Stud. Therm. Eng. 28 (2021), 101542.
[32] Asmat Ullah Yahya, Imran Siddique, Nadeem Salamat, Sohaib Abdal, Sajjad Hussain, A Numerical Investigation for Tangent Hyperbolic Hybrid Nanofluid Transportation across Riga Wedge, Waves Random Complex Media, 2022, https://doi.org/10.1080/17455030.2022.2111032.
[33] H. Thameem Basha, R. Sivaraj, Isaac L. Animasaun, "Stability analysis on Ag-MgO/water hybrid nanofluid flow over an extending/contracting Riga wedge and stagnation point, Comput. Therm. Sci. 12 (6) (2020).
[34] Danial Habib, Nadeem Salamat, Sajjad Hussain, Sohaib Abdal, Bagh Ali, Insight of Riga Effects on Dynamic of Prandtl Nanofluid over a Moving Wedge via Keller Box Approach, Waves Random Complex Media, 2022, https://doi.org/10.1080/17455030.2022.2111034.
[35] Imran Siddique, Yasir Khan, Muhammad Nadeem, Awrejcewicz Jan, Muhammad Bilal, Significance of heat transfer for second-grade fuzzy hybrid nanofluid flow over a stretching/shrinking Riga wedge, AIMS Mathematics 8 (1) (2023) 295–316.

[36] H.A. El-dawy, Rama Subba Reddy Gorla, The flow of a micropolar nanofluid past a stretched and shrinking wedge surface with absorption, Case Stud. Therm. Eng. 26 (2021), 101005.
[37] V.M. Falkner, S.W. Skan, Some approximate solutions of the boundary-layer for flow past a stretching boundary, SIAM J. Appl. Math. 46 (1931) 1350–1358.
[38] D.R. Hartree, On equation occurring in Falkner and Skan's approximate treatment of the equations of the boundary layer, Proc. Camb. Phil. Soc. 33 (1937) 323–329.
[39] K.A. Yih, MHD forced convection flow adjacent to a non-isothermal wedge, Int. Commun. Heat Mass Tran. 26 (6) (1999) 819–827.
[40] A. Ishak, R. Nazar, I. Pop, Falkner-Skan equation for flow past a moving wedge with suction or injection, J Appl Math Comput 25 (2007) 67–83.
[41] Nor Azizah Yacob, Anuar Ishak, Ioan Pop, Falkner–Skan problem for a static or moving wedge in nanofluids, Int. J. Therm. Sci. 50 (2011) 133–139.
[42] Masood Khan Hashim, Impact of heat transfer analysis on Carreau fluid-flow past a static/moving wedge, Therm. Sci. 22 (2018) 809–820.
[43] X. Xu, S. Chen, Dual solutions of a boundary layer problem for MHD nanofluids through a permeable wedge with variable viscosity, Bound. Value Probl. 2017 (1) (2017) 1–13.
[44] S.R. Sayyed, B.B. Singh, N. Bano, Analytical solution of MHD slip flow past a constant wedge within porous medium using DTM-Pade, Appl. Math. Comput. 321 (2018) 472–482.
[45] I.S. Awaludin, A. Ishak, I. Pop, On the stability of MHD boundary layer flow over a stretching/shrinking wedge, Sci. Rep. 8 (2018), 13622.
[46] W. Ibrahim, A. Tulu, Magnetohydrodynamic (MHD) boundary layer flow past a wedge with heat transfer and viscous effects of nanofluid embedded in porous media, Math. Probl Eng. 450 (2019) 7852.
[47] J.H. Merkin, A model for isothermal homogenous-heterogeneous reactions in boundary layer flow, Math. Comput. Model. 24 (1996) 125–136.
[48] N.L. Xu, H. Xu, A. Raees, Homogeneous–heterogeneous reactions in flow of nanofluids near the stagnation region of a plane surface: the Buongiorno's model, Int. J. Heat Mass Tran. 125 (2018) 604–609.
[49] T. Hayat, M. Rashid, A. Alsaedi, Three dimensional radiative flow of magnetite-nanofluid with homogeneous–heterogeneous reactions, Results Phys. 8 (2018) 268–275.
[50] M. Imtiaz, F. Mabood, T. Hayat, A. Alsaedi, Homogeneous– heterogeneous reactions in MHD radiative flow of second grade fluid due to a curved stretching surface, Int. J. Heat Mass Tran. 145 (2019), 118781.
[51] M. Waqas, A mathematical and computational framework for heat transfer analysis of ferromagnetic non-Newtonian liquid subjected to heterogeneous and homogeneous reactions, J. Magn. Magn Mater. 493 (2020), 165646.
[52] V. Singh, V.K. Yadav, V. Mishra, Nanotechnology: an application in biofuel production, in: M. Srivastava, N. Srivastava, P. Mishra, V. Gupta (Eds.), Nanomaterials in Biofuels Research. Clean Energy Production Technologies, Springer, Singapore, 2020, https://doi.org/10.1007/978-981-13-9333-4_6.
[53] Patrick T. Sekoai, Cecil Naphtaly Moro Ouma, Stephanus Petrus du Preez, Phillimon Modisha, Nicolaas Engelbrecht, Dmitri G. Bessarabov, Anish Ghimire, Application of nanoparticles in biofuels: an overview, Fuel 237 (2019) 380–397.
[54] Michael G. Bidir, N.K. Millerjothi, Muyiwa S. Adaramola, Ftwi Y. Hagos, The role of nanoparticles on biofuel production and as an additive in ternary blend fuelled diesel engine: a review, Energy Rep. 7 (2021).
[55] S. Chandra Kishore, S. Perumal, R. Atchudan, A.K. Sundramoorthy, M. Alagan, S. Sangaraju, Y.R. Lee, A review of biomass-derived heterogeneous catalysts for biodiesel production, Catalysts 12 (2022) 1501.
[56] Di Martino Serio, et al., Heterogeneous catalysts for biodiesel production, Energy Fuels 22 (1) (2008) 207–217.
[57] P. Sudarsanam, R. Zhong, S. Van den Bosch, S.M. Coman, V.I. Parvulescu, B.F. Sels, Functionalised heterogeneous catalysts for sustainable biomass valorisation, Chem. Soc. Rev. 47 (2018) 8349–8402.
[58] D. Kumar, S. Sharma, N. Srivastava, S. Shukla, K. Gaurav, Advancement in the utilization of nanocatalyst for transesterification of triglycerides, J. Nanosci. Tech. 4 (2018) 374–379.
[59] B. Mallesham, P. Sudarsanam, B.M. Reddy, Production of biofuel additives from esterification and acetalization of bioglycerol over SnO_2-based solid acids, Ind. Eng. Chem. Res. 53 (2014) 18775–18785.
[60] X.L. Zhang, S. Yan, R.S. Tyagi, R.Y. Surampalli, Biodiesel production from heterotrophic microalgae through transesterification and nanotechnology application in the production, Renew. Sustain. Energy Rev. 26 (2013) 216–223.
[61] K. Palaniappan, An overview of applications of nanotechnology in biofuel production, World Appl. Sci. J. 35 (2017) 1305–1311.
[62] I. Khan, K. Saeed, I. Khan, Nanoparticles: properties, applications and toxicities, Arab. J. Chem. 12 (2019) 908–931.
[63] P. Sudarsanam, R. Zhong, S. Van den Bosch, S.M. Coman, V.I. Parvulescu, B.F. Sels, Functionalised heterogeneous catalysts for sustainable biomass valorisation, Chem. Soc. Rev. 47 (2018) 8349–8402.
[64] D. Kumar, S. Sharma, N. Srivastava, S. Shukla, K. Gaurav, Advancement in the utilization of nanocatalyst for transesterification of triglycerides, J. Nanosci. Tech. 4 (2018) 374–379.
[65] B. Mallesham, P. Sudarsanam, B.M. Reddy, Production of biofuel additives from esterification and acetalization of bioglycerol over SnO_2-based solid acids, Ind. Eng. Chem. Res. 53 (2014) 18775–18785.
[66] A. Zuliani, F. Ivars, R. Luque, Advances in nanocatalysts design for biofuels production, ChemCatChem 10 (2018) 1968–1981.